FEASIBILITY FOR ORBITAL LIFE EXTENSION OF A CUBESAT FLYING IN THE LOWER THERMOSPHERE

by

Nicolás Martínez Baquero

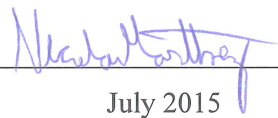A Thesis

Submitted to the Faculty of the

WORCESTER POLYTECHNIC INSTITUTE

in partial fulfillment of the requirement for the degree of

Master of Science
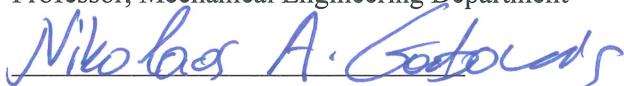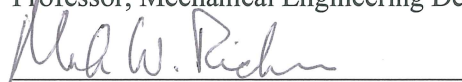
in

Mechanical Engineering

July 2015

APPROVED:

Dr. John J. Blandino, Co-Advisor
Associate Professor, Mechanical Engineering Department

Dr. Michael A. Demetriou, Co-Advisor and Committee Member
Professor, Mechanical Engineering Department

Dr. Nikolaos A. Gatsonis, Co-Advisor and Committee Member
Professor, Mechanical Engineering Department

Dr. Mark W. Richman, Graduate Committee Representative
Associate Professor, Mechanical Engineering Department

Abstract

Orbital flight of CubeSats in extremely Low Earth Orbit, defined here as an altitude between 150 – 250 km, has the potential to enable a wide range of missions in support of atmospheric measurements, national security, and natural resource monitoring. In this work, a mission study is presented to demonstrate the feasibility of using commercially available sensor and electric thruster technology to extend the orbital lifetime of a 3U CubeSat flying at an altitude of 210 km. The CubeSat consists of a 3U configuration and assumes the use of commercially available sensors, GPS, and electric power systems. The thruster is a de-rated version of a commercially available electrospray thruster operating at 2 W, 0.175 mN thrust, and an Isp of 500 s. The mission consists of two phases. In Phase I the CubeSat is deployed from the International Space Station orbit (414 km) and uses the thruster to de-orbit to the target altitude of 210 km. Phase II then begins during which the propulsion system is used to extend the mission lifetime until propellant is fully expended. A control algorithm based on maintaining a target orbital energy is presented in which simulated GPS updates are corrupted with measurement noise to simulate state data which would be available to the spacecraft computer. An Extended Kalman Filter is used to generate estimates of the orbital dynamic state between the 1 Hz GPS updates, allowing thruster control commands at a frequency of 10 Hz. For Phase I, operating at full thrust, the spacecraft requires 25.21 days to descend from 414 to 210 km, corresponding to a $\Delta V = 96.25$ m/s and a propellant consumption of 77.8 g. Phase II, the primary mission phase, lasts for 57.83 days, corresponding to a $\Delta V = 119.15$ m/s during which the remaining 94.2 g of propellant are consumed.

Acknowledgments

"Earth is the cradle of humanity, but one cannot live in a cradle forever."

- Konstantin Tsiolkovsky

Table of Contents

List of Figures

List of Tables

Nomenclature

a = semi-major axis, km

$\mathbf{a}_d$ = acceleration due to atmospheric drag, km/s^2

$\mathbf{a}_{ns}$ = acceleration due to aspherical geopotential, km/s^2

$\mathbf{a}_T$ = control acceleration vector, km/s^2

C = controller gain

C_d = drag coefficient

E_t = target energy per unit mass, km^2/s^2

E_e = estimated energy per unit mass, km^2/s^2

E_{SA} = energy generated by solar arrays, J

F = Jacobian of non-linear model

g = mean anomaly of the sun, degrees

G = state matrix of process noise

H_k = Jacobian of measurement model

i = orbital inclination, deg

$\bar{K}_k$ = Kalman gain

L = mean longitude of the sun, degrees

$m(t)$ = spacecraft mass, kg

$m_{p,0}$ = initial propellant mass, kg

$\dot{m}(t)$ = mass flow rate, mg/s

n = number of days since J.2000.0

P_{EP} = power available for electric propulsion system, W

$P_{S/C}$ = power available for spacecraft bus and payload, W

P_k = covariance matrix of residual noise

Q = covariance of process noise

R_E = equatorial radius of Earth, km

$\mathbf{r}_t$ = target position vector, km

$\mathbf{r}_e$ = estimated position vector, km

$\mathbf{r}_a$ = actual position vector, km

$\hat{\mathbf{R}}_c$ = unit CubeSat position vector

R_s = distance to the sun, AU

$\hat{\mathbf{R}}_s$	= unit earth-sun vector
S	= reference area, 0.01 m^2
T_d	= time spent in sunlight during one orbital period, s
T_e	= time spent in eclipse during one orbital period, s
T_T	= commanded thrust in the along-track direction, mN
W	= work done by atmospheric drag, J
$\mathbf{v}_t$	= target velocity of the spacecraft, km/s
$\mathbf{v}_e$	= estimated velocity of the spacecraft, km/s
$\mathbf{v}_a$	= actual velocity of the spacecraft, km/s
$\mathbf{v}_{rel}$	= velocity of the spacecraft relative to the atmosphere, km/s
$\mathbf{x}_a$	= actual state, 6x1
$\mathbf{x}_e$	= estimated state, 6x1
X_d	= power transfer efficiency: solar array to loads
X_e	= power transfer efficiency: solar array to batteries
$\mathbf{y}_k$	= GPS state measurement, 6x1
ΔE	= energy per unit mass error, km^2/s^2
ΔV	= change in velocity, m/s
Δt	= integration time step, 0.1 sec.
δ	= declination (latitude), radians
$\delta\mathbf{r}$	= error between estimated and actual position, m
$\delta\dot{\mathbf{r}}$	= error between estimated and actual velocity, cm/s
ε	= eccentricity
ε_s	= obliquity of the ecliptic of the sun, degrees
$\boldsymbol{\varepsilon}_{GPS,k}$	= GPS uncertainty vector, 6x1
$\boldsymbol{\varepsilon}_T$	= thrust acceleration uncertainty, m/s^2
θ	= true anomaly, deg
ρ	= atmospheric density, kg/m^3
λ	= ecliptic longitude of the sun, degrees
ω	= argument of the perigee, deg
$\omega_\oplus$	= angular velocity of Earth, rad/s

1. Introduction

O RBITAL flight at low altitudes of $150 - 250$ km, defined for this work as extremely Low Earth Orbit (eLEO), has the potential to enable a wide range of missions with applications related to national security as well as real-time monitoring of atmospheric phenomena and natural resources. Due to their relatively low cost to build and launch, the use of nanosatellites (mass < 10 kg) for this type of mission further lowers the barrier to access to space for governmental, academic, and private industry participants.

In recent years, CubeSats have emerged as a potential alternative to traditional satellite platforms for commercial resource monitoring and telecommunication. For example, the San Francisco-based company Planet Labs has launched dozens of CubeSats for the purpose of imaging the Earth's surface, and makes this data accessible to businesses involved in energy production, natural resource mapping, etc[1]. Planet Labs' satellites capture images with a resolution of 3 to 5 m, from 52° inclination, 400 km, near-circular orbits. However, the resolution of the images obtained is not sufficient for certain applications. For example, the construction industry uses remote sensing for monitoring of resources used in the design of infrastructure, and accurate maps of the terrain are needed, including Digital Terrain Modeling (DTM). Resolution needs to be on the order of 0.2 m[2], which cannot be accomplished with Planet Labs' current combination of instrument and altitude. This problem can be solved by decreasing the orbital altitude of the spacecraft. Conversely, for a given resolution, the size and mass of the imaging equipment can be reduced by decreasing the orbital altitude. An analysis conducted by Thales Alenia Space reveals that for a resolution of 1 m, a spacecraft with an orbital perigee of 160 km would allow "a four times reduction in the required aperture diameter and focal length, when compared to an optical imaging satellite at 650 km of altitude" [1], furthermore, the transmission power for the downlink would be reduced by a factor of 10.

---

[1] Data available online at http://www.planetlabs.com/impact [accessed 15 April 2015]

[2] Data available online at http://www.daedalus-se.com/cubesats-suitable-remote-sensing/ [accessed 21 March 2015]

Moreover, CubeSat flight in eLEO is relevant to the support of science missions of interest to NASA and other organizations. CubeSats orbiting in eLEO could provide in-situ observations of the lower thermosphere using miniaturized payloads, such as the miniature spectrometers currently under development by the Heliophysics Science Division at NASA's Goddard Space Flight Center NASA's Goddard Spaceflight Center (GSFC). The transition region between 150 km and 300 km encompasses a zone where much of the energy from the solar wind couples to the Earth's upper atmosphere, and yet remains greatly unexplored. Sounding rockets provide only brief glimpses of the physics, and ground radars do not measure all of the parameters, especially at smaller scale sizes.

Orbital flight in the transition region has mainly been exploited for geodesy and oceanography research purposes, with flight at lower altitudes enabling higher accuracy in mapping of the geoid. Within the last decade, three missions have performed detailed gravimetric measurements. The German CHAllenging Micro-satellite Payload for geophysical research and application (CHAMP) satellite [2] was launched in 2000 to a mean altitude of $\approx$ 450 km, decaying to 296 km at the time of its reentry in 2010. In 2002, the pair of satellites comprising the Gravity Recover and Climate Experiment (GRACE) was launched to an altitude of 485 km where they remain active as of 2015. Finally, the European Space Agency (ESA) launched the Gravity and Steady-State Ocean Circulation Explorer (GOCE) spacecraft [3] in 2009 to an altitude of $\approx$ 280 km. Most of the mission science was collected at an altitude of 255 km, which was followed by a series of planned descents as part of a low-orbit operations campaign. The final, low–orbit operations were performed at 224 km, where science collection continued prior to mission end and re-entry in 2013 [4]. All three of these spacecraft employed some variant of the Space Three-axis Accelerometer for Research (STAR) instrument to measure non-gravitational acceleration [5]. The STAR gravitational reference sensor (GRS) uses a freely floating proof mass which is shielded inside the spacecraft from non-conservative forces such as atmospheric drag, magnetic disturbances, solar radiation, etc. The position of the proof mass is actively monitored within an electrostatic cage, allowing very precise measurement of the external disturbances. Of these three missions, only GOCE was designed to operate in a so-called "drag-

free" mode, in which an ion propulsion system uses GRS data to adjust thrust level and continuously compensate for drag, solar radiation pressure, and any non-gravitational acceleration along the in-track direction [6]. Drag-free operation has been investigated as a possible follow-on option for the GRACE mission as well [7]. To achieve drag-free flight within the mass, power, and volume restrictions of a CubeSat is extremely challenging. Conklin et al. [8] investigated the feasibility of a drag-free, 3U CubeSat, equipped with a 1U GRS and a cold gas micro-propulsion system to maintain the spacecraft position with respect to the proof mass. In that study, the mission lifetime as a function of altitude was evaluated using a cold-gas thruster built by VACCO Space Products, with a maximum thrust of 55 mN, Isp of 65 sec, and a total impulse capability of 24 N-sec. The proposed mission scenario assumed an average altitude of 400 km with a lifetime of approximately 70 days. As a point of comparison with the present work, the lifetime at an altitude of 210 km was approximately 4 days [8].

Long-duration flight in the lower thermosphere is extremely challenging, mainly due to substantial aerothermodynamic loads. At these altitudes, atmospheric drag results in severely shortened lifetime followed by de-orbiting. Thus, the use of on-board propulsion, even for a non-drag-free spacecraft, is essential. The severe constraints in mass, power and volume associated with a CubeSat make use of any propulsion system extremely challenging. In this work we demonstrate the feasibility of using relatively mature technology (TRL > 4, i.e. "component or breadboard demonstrated in a laboratory environment") to enable extended CubeSat mission life in the lower thermosphere. For the purposes of this study, the mission requirement is defined as maintaining a (mean) "target altitude" for as long as possible.

The propulsion controller is designed based on the principle of conservation of mechanical energy. The forces acting on the CubeSat are conservative, with the exception of the atmospheric drag force. The energy of the target orbit, which would be selected to support specific science, commercial, or defense-related objectives, is specified at the beginning of the simulation. The instantaneous orbital energy is calculated based on GPS data in order to calculate an energy 'error' which is used to generate the thrust for

orbit maintenance. GPS state measurements are inherently noisy. Hence, an Extended Kalman Filter was implemented to reduce the uncertainty in the energy estimates.

For the range of altitude corresponding to eLEO, where the propulsion system is continuously used to counteract drag forces, the thruster will need throttling capability. Previous authors have reviewed propulsion options available for CubeSats [9], [10]. For the purpose of this study, a baseline thruster was selected that could be accommodated within 1U of a 3U CubeSat and that could provide sufficient thrust (0.1 – 1.0 mN) at low power (< 5W) to counteract the effect of drag at the altitude of interest. The actuator baseline for this work will produce thrust in the along-track direction, and consists of a single Busek Electrospray Thruster System (BET-1)[3].

This thesis is organized as follows. In Chapter 2, the orbital dynamics of a CubeSat mission are modeled. The orbital dynamics include two-body gravity effects and perturbations such as J2-J6 non-spherical geopotential effects. The controller system design is presented in Chapter 3. The spacecraft design, including a description of the power and propulsion systems, is presented in Chapter 4. A 3U CubeSat platform and commercially available subsystems, such as sun sensors, GPS receiver, magnetorquers, etc. are considered. The results are presented in Chapter 5 to demonstrate the effectiveness of the proposed controller and actuator in maintaining the target altitude in eLEO. Finally, Chapter 6 presents conclusions and recommendations for continued work.

1.1. The CubeSat state-of-the-art

A CubeSat is a miniaturized satellite developed in 1999 by Bob Twiggs, from Stanford University, and Jordi Puig-Suari, from the California Polytechnic State University (CalPoly), San Luis Obispo, with the goal of allowing college students to design, build and operate affordable spacecraft with similar

---

[3] Data available online at http://www.busek.com/index_htm_files/70008500G.pdf [accessed 20 April 2015]

capabilities to the first satellite, Sputnik[4]. A CubeSat unit (1U) has a volume of 1 liter, 10x10x10 cm dimensions, and a mass of less than 1.33 kg. The CubeSat standard permits larger 2U (10x10x20 cm) and 3U (10x10x30 cm) sizes, which are scalable along one axis. 6U and 12U CubeSats have been designed but have not flown to space yet. While CubeSats were originally devised for increasing the access to space to academia, they have been embraced by other communities and agencies, including NASA and the Air Force, because of their affordability and flexibility compared to traditional spacecraft.

Approximately 330 CubeSats have flown to date[5]. Nanosatellites (i.e. having a mass < 10 kg) have been used for a wide range of scientific and commercial uses all over the world. CubeSats such as the RAX-2 [11] mission, developed by the University of Michigan to study plasma irregularities in the ionosphere, and CANX-2, which carried an atmospheric spectrometer to measure greenhouse gases [12], are examples of the current interest in using CubeSats for serious scientific investigations. Furthermore, CubeSats have emerged as a framework for successful commercial applications. As mentioned before, San Francisco-based company Planet Labs has launched dozens of 'doves', i.e. 3U CubeSats for imaging the Earth's surface; and a company called Spire Inc. uses CubeSats for relaying Automatic Identification System (AIS) data of ships in high seas and weather monitoring[6]. So far, missions using nanosatellites have been limited to operation in LEO, although there have been studies and proposals to fly CubeSats in lunar and interplanetary space [13], [14]. Furthermore, the first lunar nanosatellite, a 6U CubeSat developed by Morehead State University called IceCube, is slated to fly in the first Space Launch System (SLS) flight (EM-1). IceCube will be deployed in lunar trajectory by the SLS and is designed to look for water ice and other lunar volatiles[7].

---

[4] Obtained from interview to Jordi Puig-Suari, available online at http://spacenews.com/jordi-puig-suari-co-founder-tyvak-nano-satellite-systems-llc/
[5] Data available online at http://sites.google.com/a/slu.edu/swartwout/home/cubesat-database [accessed 21 April 2015]
[6] Data available online at http://www.spire.com/products/. [accessed 22 May 2015
[7] Data available online at https://shar.es/12a824. [accesed 22 May 2015]

1.2. Orbital flight in eLEO

A spacecraft orbiting the earth in eLEO would fly through the lower thermosphere, a layer of the atmosphere that is above the mesosphere and below the exosphere[8]. Along with the earth's oblateness, atmospheric drag has the largest influence in orbital flight at low altitudes. Atmospheric drag forces are not conservative, they continuously reduce the orbital energy of the spacecraft. Without the use of propulsion, atmospheric drag acting on a spacecraft results in orbital decay, followed by reentry and disintegration above the Kármán line (100 km of altitude). Direct Simulation Monte Carlo (DSMC) drag analysis by Marchetti et al [7] show that the local neutral particle mean free paths range from 20 – 30 m at an altitude of 160 km to 200 – 270 m at an altitude of 225 km. For a characteristic length of 1.942 m these mean free paths correspond to Knudsen numbers ranging from a value on the order of 10, for the 160 km case, to the order of hundreds for higher altitudes. Hence, because of the high Knudsen numbers associated with flight in eLEO, the continuum assumption is invalid and the freestream flow is considered to be in the free molecular flow regime.

The aforementioned commercial and atmospheric science applications of orbital flight at low altitude are the objective of future missions. Flight in eLEO has mainly been exploited for geodesy and oceanography research purposes. Spacecraft equipped with gravitational reference sensors (GRS) can accurately measure the gravitational field of the earth by measuring the changes in orbital elements due to gravitational perturbations. The force of gravity is non-uniform due to the earth's rotation, ocean circulation, and non-uniform mass distribution within the earth's interior. The gravitational field is stronger at low altitudes, and operation in eLEO allows more accurate gravitational mapping at the cost of increased drag. Spacecraft designed for geodesy missions in eLEO can be designed to be drag-free in order to avoid the necessity of correcting for uncertainties of atmospheric drag and solar pressure [15]. "Drag-free" refers

---

[8] The mesosphere extends from 50 km above the Earth's surface to 85 km. The exosphere is the outermost layer of the atmosphere, it extends from 600 km to 10,000 km above the Earth. Data available online at http://www.srh.noaa.gov/jetstream/atmos/layers.htm [accesed 20 May 2015]

to the continuous cancelation of external disturbances on the spacecraft. In one form of gravitational sensors, in which acceleration is carefully measured, freely floating proof masses inside the spacecraft are shielded from non-conservative forces such as atmospheric drag, magnetic disturbances, solar radiation pressure, etc.

The spacecraft's controller activates the propulsion system to keep it centered on the proof masses, subjected only to gravitational forces [7]. The motion of the proof masses is used to find the anomalies and variations of the Earth's gravitational field. The European Space Agency (ESA) launched the Gravity and Steady-State Ocean Circulation Explorer (GOCE) spacecraft in 2009, with the goal of conducting the most advanced gravimetric mission to date. GOCE was equipped with an Electrostatic Gravity Gradiometer (EGG), designed by the French Aerospace Lab (ONERA) to measure the three components of the gravity gradient tensor. The EGG principle of operation is described by Drinkwater et al [6]:

> " EGG is a three-axis gradiometer consisting of 3 pairs of three-axis servo-controlled capacitive accelerometers on an ultra-stable carbon-carbon structure, a six degree of freedom servo-controlled electrostatic suspension provides control of the proof mass in terms of translation and rotation. A pair of identical accelerometers, mounted on the ultra-stable structure 50 cm apart, form a "gradiometer arm". The difference between accelerations measured by each of the two accelerometers, in the direction joining them, is the basic gradiometric datum."

GOCE effectively demonstrated drag-free control, advanced drag compensation was achieved with ion-propulsion technology [6]. Figure 1 shows an artists's rendition of GOCE.
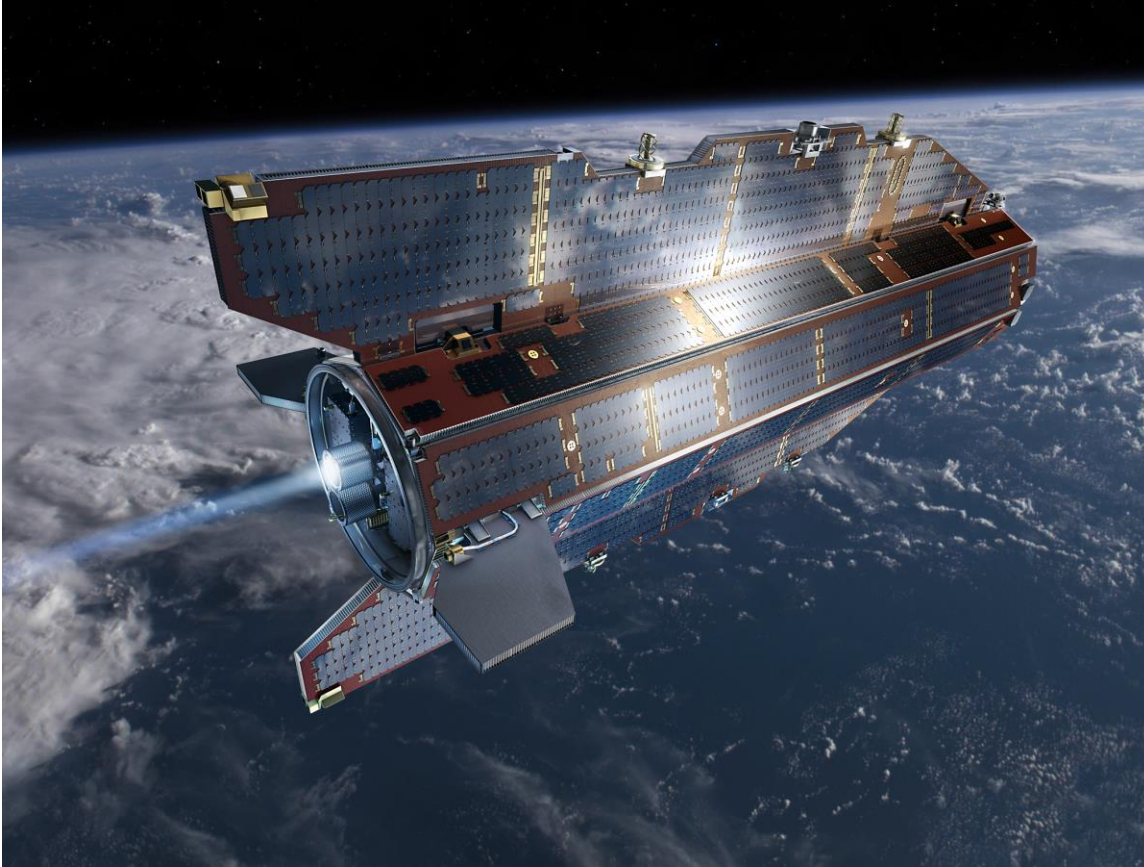
Figure 1: GOCE Spacecraft, Source: ESA [16]

1.3. Present Study

In this investigation, the dynamics of a 3U CubeSat are modeled. Spacecraft dynamics include the two-body gravitational effects and a sixth-order approximation of the gravitational perturbations due to the non-spherical geopotential of Earth. The airflow around spacecraft in the lower thermosphere is modeled as near-free molecular flow due to the large Knudsen numbers at high altitudes. It is assumed that the atmospheric drag force is proportional to the square of the velocity of the spacecraft. Low orbit maintenance (LOM) is conducted continuously using low-thrust, electrospray colloid propulsion.

The propulsion controller is designed based on the principle of conservation of mechanical energy. The forces acting on the CubeSat are conservative, with the exception of the atmospheric drag force, which

performs work on the spacecraft and reduces its orbital energy. An 'error' in energy is defined; between a constant, target energy and the estimated energy of the spacecraft, obtained from sensor measurements. The control law generates a signal that is proportional to the energy error in order to counteract the drag forces. The controller accounts for the maximum and minimum thrust available, assuming that a constant power of 2 W is available for the propulsion system at all times, as explained in section 4.2. The analysis of the results focus on the controller performance, change in the orbital elements due to perturbations and the effect of the input parameters on the duration of the orbital life extension.

2. Dynamics Modeling

2.1. Reference Frames

Two coordinate frames are used in this study: the geocentric-equatorial frame (*GCI*) and the satellite-centered rotating frame (*NTW*). The equations of motion and the state errors are calculated in the inertial *GCI* frame. The origin of the *NTW* frame is located at the center of mass of the CubeSat. The along-track, or *T* axis, is collinear with the spacecraft velocity vector. The cross-track, or *W* axis, is orthogonal to the orbital plane and parallel to the angular momentum vector ($\mathbf{h} = \mathbf{r} \times \mathbf{V}$). The *N* axis completes the orthonormal set, and is perpendicular to both *T* and *W* axes ($\mathbf{N} = \mathbf{W} \times \mathbf{T}$). The thrust acceleration is calculated in the *NTW* frame, since the thruster is mounted on the spacecraft. However, the thrust acceleration is transformed from the *NTW* to the *GCI* frame in order to solve the orbital equations of motion. Figure 2 shows the *GCI* and *NTW* frames.

2.2. Orbital Dynamics

The representation of the full dynamic state of the spacecraft requires careful attention. As part of this study, two different equations of motion are propagated and three distinct state vectors, the Target, Actual, and Estimated, are used. These are described below.

Target state: In this work the objective is to maintain a specified mean altitude. The target state represents an idealized orbit, where the CubeSat's motion is governed solely by the earth's gravitational field. The target state characterizes an orbit that has the desired mean altitude, selected on the basis of mission objectives. The "target energy," which is constant for this idealized orbit and is only subject to conservative forces, is calculated based on the target state information. It is worth noting that this state is propagated in the simulation just as a reference state, to quantify the degree to which a real CubeSat orbit in the lower thermosphere, using the actuator and controller system described, satisfies the requirement to maintain the desired altitude. Note that this is different from a so-called "drag-free" mission scenario. In a
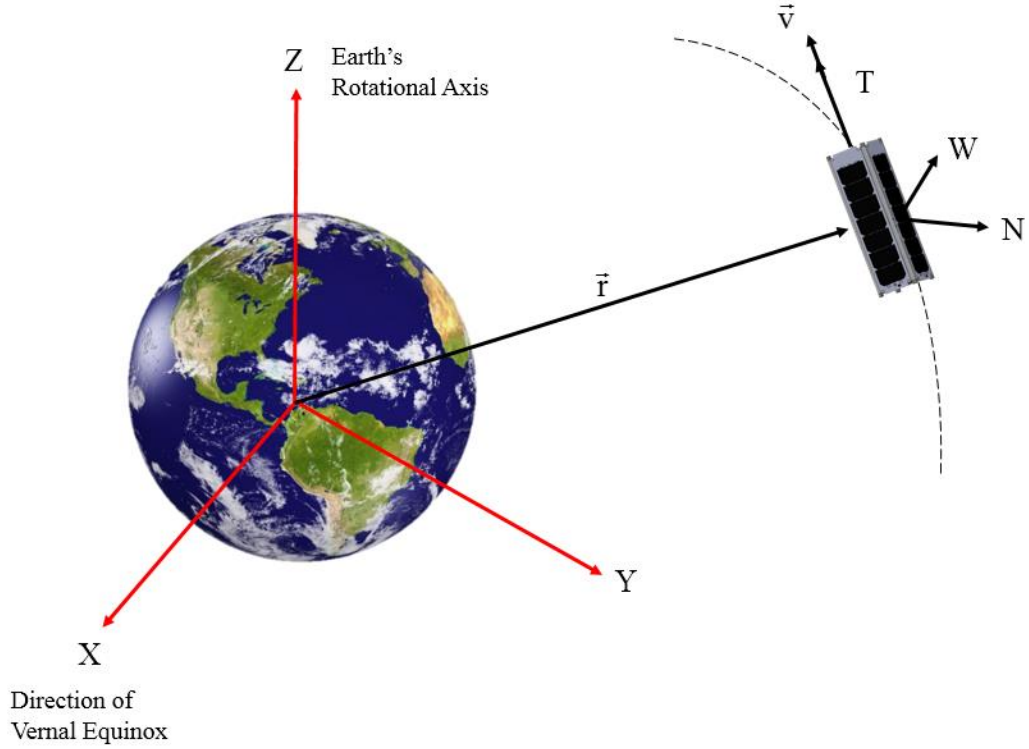
Figure 2: Reference frames

drag-free mission, the thrusters would continuously cancel drag forces. A true drag-free spacecraft requires full control to counteract drag forces along all three axes. Because of limitations in power, volume and mass, a 3U, drag-free CubeSat as described by Conklin et al. [8] presents significant challenges and requires a specialized gravitational reference sensor (GRS) to provide control input to the propulsion system. The equation of motion for the target state is given by Eq. (1),

$$\ddot{\mathbf{r}}_t(t) = -\mu \cdot \frac{\mathbf{r}_t(t)}{\left\|\mathbf{r}_t(t)\right\|^3} + \mathbf{a}_{ns,t}(t) \tag{1}$$

where $\ddot{\mathbf{r}}_t(t)$ is a 3×1 vector representing the acceleration in the *GCI* frame. The perturbations due to the non-spherical geopotential are represented with the term $\mathbf{a}_{ns,t}(t)$. The non-spherical acceleration terms are obtained from a simplified model for the zonal harmonics (J_2-J_6) acceleration terms by Vallado [17].

Actual State: The "actual" state represents the 'real' state of the spacecraft (i.e. the plant state). The state information available to the spacecraft computer will include measurement uncertainties, and so the actual state would be equivalent to the measured state only if the measurements were continuously available and subject to no uncertainty. The actual state is used in this simulation for the purpose of providing the basis for the GPS data available to the controller. In the simulation, the actual state data is corrupted with sensor noise, following a procedure that will be described. The actual state is also used to assess the quality of the solution, since the difference between the actual state and the target state represents how closely the control and actuator system are able to maintain the desired mean altitude. The actual state equation of motion is given by Eq. (2).

$$\ddot{\mathbf{r}}_a(t) = -\mu \frac{\mathbf{r}_a(t)}{\|\mathbf{r}_a(t)\|^3} + \mathbf{a}_{ns,\mathrm{a}}(t) + \mathbf{a}_{d,\mathrm{a}}(t) + \mathbf{a}_{T,\mathrm{a}}(t) \tag{2}$$

The non-spherical acceleration term $\mathbf{a}_{ns,\mathrm{a}}(t)$ also includes the J_2-J_6 perturbations, and the actual thrust acceleration $\mathbf{a}_{T,a}(t)$ differs from the estimated thrust acceleration due to the addition of uncertainty in the thruster response, as will be described in section section 4.2.

Estimated State: As will be described in detail in section 3.2, the estimated state represents the state as calculated by the on-board computer (OBC) using an Extended Kalman Filter. This state incorporates the GPS state updates, which are corrupted by noise and uncertainty, and are only available to the OBC at discrete times

2.3. Atmospheric Drag

In this simulation, the drag acceleration is assumed to be proportional to the local atmospheric density and to the square of the spacecraft velocity. The drag acceleration term shown in Eq.(2) is defined as:

$$\mathbf{a}_d(t) = -\frac{1}{2}\left(\frac{C_d S \rho(t)}{m(t)}\right)\|\mathbf{V}_{rel}(t)\|^2 \frac{\mathbf{V}_{rel}(t)}{\|\mathbf{V}_{rel}(t)\|} \tag{3}$$

where $\mathbf{V}_{rel}(t)$ is the velocity vector of the spacecraft with respect to the atmosphere, assuming that the atmosphere co-rotates with the Earth. C_d is the drag coefficient. The instantaneous spacecraft mass $m(t)$, is time dependent as propellant mass is consumed. The parameter S, or drag area, is equivalent to the cross sectional area of the spacecraft.

3. Propulsion Controller Design

As noted in the Introduction, the mission investigated for this work does not assume the spacecraft is flying drag-free. This work assumes a thruster and sensor, in this case a GPS system, which is commercially available. For this reason, an indirect measurement of the drag acceleration must be performed, as outlined in section 3.1.

3.1. Energy – based Controller

The goal of the controller is to perform continuous orbital maintenance by counteracting the effect of atmospheric drag on the CubeSat. As described in the introduction, the objective is to maintain an orbit which has a mean altitude equal to that of the target orbit for as long as possible. Thrust is only applied in the T direction as shown in Figure 9, which is collinear with the velocity vector. While there are drag forces in the cross-track and normal directions, these forces are at least one order of magnitude lower than the drag force in the along-track direction, and hence do not pose a problem from an orbital lifetime standpoint, provided the vehicle can maintain the correct orientation, i.e. possess weathercock stability. This will be discussed in section 4.4.

The controller design is based on the following principle: the gravitational (two-body and non-spherical) forces acting on the CubeSat are conservative, while the atmospheric drag force is not. Therefore, any decrease in orbital energy must be a consequence of atmospheric drag. The general form of the specific orbital energy, in terms of the non-spherical geopotential zonal harmonics, is given by Eq. (4):

$$E_e = \frac{1}{2}V_e^2 - \frac{\mu}{r_e}\left[1 - \sum_{l=2}^{\infty} J_l\left(\frac{R_E}{r_e}\right)^l P_l(\sin\delta_e)\right] \tag{4}$$

In this equation, J_l is the zonal coefficient, P_l represents the associated Legendre polynomial of degree l, δ_e is the declination (latitude) of the spacecraft, r_e and v_e are the magnitudes of the estimated position and velocity, respectively [18]. The orbital energy is calculated periodically based on GPS derived state data. Any difference, or loss, in the estimated energy of the CubeSat must arise from the effects of atmospheric

drag. The energy 'error' is calculated between the target state energy (which will be a constant) and the estimated energy, as

$$\Delta E = E_t - E_e \tag{5}$$

The atmospheric drag performs work on the CubeSat and over a sufficiently short period of time the atmospheric drag work can be estimated as:

$$W = \left\| \mathbf{F}_{D,\mathrm{T}} \right\| \left\| \mathbf{V}_e \right\| \Delta t \tag{6}$$

where $\mathbf{F}_{D,T}$ is the drag force on the CubeSat in the along-track direction. Dividing Eq. (6) by the mass of the CubeSat results in the specific work done on the CubeSat over a time interval Δt

$$\frac{W}{m} = \Delta E = a_{d,e} V_e \Delta t \tag{7}$$

Eq. (5) and Eq. (7) are equivalent expressions. Solving for the estimated drag acceleration $a_{d,e}(t)$, Eq. (8) is obtained as

$$a_{d,e} = \frac{\Delta E}{V_e \Delta t} \tag{8}$$

Eq. (8) shows how the drag acceleration is estimated using GPS data, assuming access to the full state of the spacecraft. The energy error is used as feedback to the controller to estimate the acceleration needed to maintain the orbital energy. The control acceleration vector (in the *NTW* frame) can then be written as

$$\mathbf{a}_{T,e} = \left[\left(\mathbf{a}_{T,e} \right)_N, \left(\mathbf{a}_{T,e} \right)_T, \left(\mathbf{a}_{T,e} \right)_W \right]^T = \left(0, \quad \frac{\Delta E}{V_e \Delta t}, \quad 0 \right)^T \tag{9}$$

where the thrust in the *N* and W directions is zero, because the thruster is assumed to remain aligned with the velocity (*T*) direction. In any real system, the GPS position and velocity measurements will have noise and uncertainty associated with them. The noise considerably affects the estimation accuracy of the drag acceleration, and thus the calculation of the thrust command. In addition, GPS noise, combined with the finite time period between thrust command updates can lead to 'chattering' in the control signal and drive the commanded thrust from maximum to zero (and vice versa) over very short timescales, which is

problematic from the propulsion system performance standpoint. Consequently, Eq. (9) was modified to reduce the magnitude of the changes in thrust which occur from one time step to the next. The modification consists of assuming the commanded thrust is proportional to, rather than equal to, the estimated acceleration as given in Eq. (9). In this formulation, the commanded thrust acceleration takes the form

$$u_e = \mathbf{a}_{T,e} = \left(0, \quad C \frac{T_{\max}}{m(t)} \frac{\Delta E}{\|E_t\|}, \quad 0 \right)^T \tag{10}$$

where the energy error, ΔE, has been non-dimensionalized. $T_{\max}$ is the maximum available thrust, and C is a controller gain determined iteratively while tuning the controller. In addition to using a proportionality constant to reduce chatter, the effect of noise on the controller is further minimized with the implementation of an Extended Kalman Filter.

3.2. Continuous-Discrete Extended Kalman Filter

The extended Kalman filter (EKF) is used in a large class of orbit and attitude determination estimation problems [19]. For this work, a continuous-discrete filter is used because the equations of motion are propagated continuously in time, but the measurements are obtained at discrete times. The equation of motion of the actual spacecraft, defined in Eq.(2), is represented in state space as:

$$\mathbf{x}_a = \begin{pmatrix} \mathbf{r}_a \\ \mathbf{v}_a \end{pmatrix}, \qquad \dot{\mathbf{x}}_a = f(\mathbf{x}_a, u_a, w) \tag{11}$$

where w is the process noise of the model and is a zero-mean, Gaussian function with covariance Q, i.e. $w \sim N(0, Q)$. The GPS measurements, which provide the full state of the spacecraft, are modeled by Eq.(12)

$$\mathbf{y}_k = \mathbf{x}_{a,k} + \varepsilon_{GPS,k}, \qquad \varepsilon_{GPS,k} \sim N(0, R_k) \tag{12}$$

In this equation, $\mathbf{x}_{a,k}$ is the actual state at the kth update, and $\varepsilon_{GPS,k}$ is the measurement noise, which depends on the type of GPS receiver considered for the mission.

The estimated state calculated by the on-board computer is represented by

$$\mathbf{x}_e = \begin{pmatrix} \mathbf{r}_e \\ \mathbf{v}_e \end{pmatrix}, \qquad \dot{\mathbf{x}}_e = f(\mathbf{x}_e, \mathbf{u}_e) \tag{13}$$

The equation of motion for the spacecraft estimate state is propagated continuously. However, since GPS measurement updates take place at discrete times, there is no correction process between measurements. The equation of motion for the spacecraft estimate state, given in Eq.(14), is similar to the equation of motion for the spacecraft actual state.

$$\ddot{\mathbf{r}}_e(t) = -\mu \frac{\mathbf{r}_e(t)}{\|\mathbf{r}_e(t)\|^3} + \mathbf{a}_{ns,e}(t) + \mathbf{a}_{d,e}(t) + \mathbf{a}_{T,e}(t), \qquad t \in [t_{k-1}, t_k) \tag{14}$$

The covariance of the residual noise, P_k, is used to find the Kalman gain, and is obtained by continuously solving the matrix differential Riccati equation:

$$\dot{P} = F \cdot P + P \cdot F^T + G \cdot Q \cdot G^T \tag{15}$$

where F is the state matrix that is obtained from the linearization of the non-linear model, evaluated at the estimated state. G is the state matrix of the process noise due to the uncertainty in the estimation of the acceleration of the spacecraft. G is the 6×6 matrix shown in Eq.(16)

$$F \equiv \frac{df}{dx}\bigg|_{x_e}, \qquad G \equiv \frac{df}{dw}\bigg|_{x_e} = \begin{bmatrix} 0_{3x3} & 0_{3x3} \\ 0_{3x3} & I_{3x3} \end{bmatrix} \tag{16}$$

After evaluating F and G, the Kalman gain is calculated:

$$\bar{K}_k = P_k^- H_k^T [H_k P_k^- H_k^T + R_k]^{-1} \tag{17}$$

where P_k^- is the *a priori* covariance matrix and H_k is the Jacobian of the measurement model. Since the full state is observed, $H_k = I_{6x6}$. After the Kalman gain is calculated, the estimate of the state is corrected:

$$\mathbf{x}_{e,k}^+ = \mathbf{x}_{e,k}^- + \bar{K}_k [\mathbf{y}_k - \mathbf{x}_{e,k}^-] \tag{18}$$

Finally, the *a posteriori* covariance matrix is calculated before the next measurement update.

$$P_k^+ = [I_{6x6} - \bar{K}_k H_k] P_k^- \tag{19}$$

4. Reference Case

4.1. Atmospheric Drag Model

The drag coefficient, C_d, is assumed to be equal to 2.2 following Marchetti et al. [7] and [20]. The parameter S, is equivalent to the cross sectional area of a 1U (i.e. 0.01 m^2) CubeSat with its long axis oriented along the velocity vector. The local atmospheric density, $\rho(t)$, is provided by the MSISE-90 [21] model. The species included in the model are: O, O_2, N, N_2, Ar, He and H. The data was chosen at the peak of a solar cycle, in order to simulate a 'worst-case' scenario.

4.2. Power System

It is assumed that the CubeSat will be equipped with four body mounted solar panels. While it would be advantageous to have deployable solar panels for additional power, it is anticipated that at the altitudes of interest, the aerodynamic moments would destabilize the attitude of the spacecraft without the use of additional attitude control actuators. State-of-the-art solar panels have triple junction Gallium Arsenide cells, with an efficiency of 28.3%. Commercial-off-the-shelf (COTS) panels manufactured by Clyde Space Limited for a 3U length have up to eight cells, with a beginning-of-life (BOL) power of 8.33 W[9]. A picture of a side solar panel can be seen in Figure 3.

---

[9] Data available online at http://www.clyde-space.com/cubesat_shop/solar_panels/3u_solar_panels [accessed 14 April 2015.
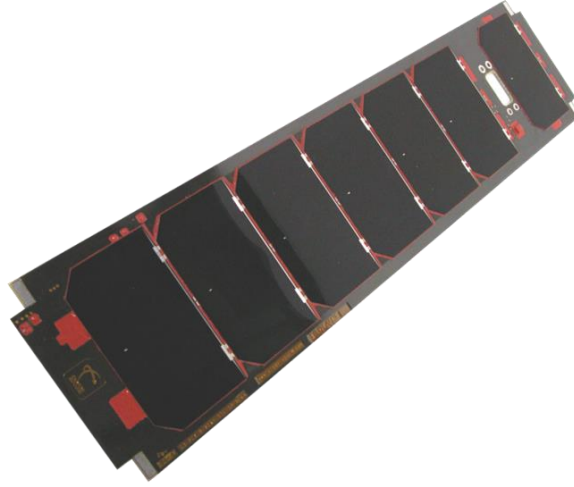
Figure 3: 3U Side Solar Panel. © 2015 Clyde Space Ltd. [22]

4.2.1. Sun Vector Calculation

The power generated by the solar cells depend on several factors: direction of the sun vector, orientation of the CubeSat with respect to the sun vector, fraction of orbital time spent in daylight and eclipse, etc. The following formulas, obtained from the Astronomical Almanac for the year 2011 [23], were used to compute the coordinates of the sun, as shown in Eq.(26), in the *GCI* frame (and hence the earth-sun vector) to a precision of 0.01°, and the time elapsed as a function of the Julian Date to a precision of 0.1 minutes between 1950 and 2050. The earth orbits around the sun, but to find the sun vector in the *GCI* frame it is convenient to suppose that sun rotates around the earth. The only necessary input is the Julian Date (*JD*), the continuous count of days since noon Universal Time on January 1, 4713 BC [23]. The parameter *n* is the number of days since J2000.0 (i.e. noon in Greenwich time, on January 1st, 2000).

$$n = JD - 2451545.0 \tag{20}$$

the parameter n is used to calculate the mean longitude of the sun, L, corrected for the aberration of light

$$L = 280.460^o + 0.9856474^o \, n \tag{21}$$

the mean anomaly, g, is also obtained as function of n

$$g = 357.528^o + 0.9856003^o \, n \tag{22}$$

The mean longitude and the mean anomaly are used to calculate the ecliptic longitude, λ.

19

$$\lambda = L + 1.915^o \sin g + 0.020^o \sin 2g \tag{23}$$

the obliquity of the ecliptic, ε_s, represents the angular distance of the sun along the ecliptic from the vernal equinox, given by

$$\varepsilon_s = 23.439^o - 0.0000004^o n \tag{24}$$

the distance from the earth to the sun, R_s, in astronomical units (AU), can then be calculated

$$R_s = 1.00014 - 0.01671 \cos g - 0.00014 \cos 2g \tag{25}$$

finally, the components of the earth-sun vector in the *GCI* frame, in AU, are given by:

$$\begin{aligned} x &= R_s \cos \lambda \\ y &= R_s \cos \varepsilon_s \sin \lambda \\ z &= R_s \sin \varepsilon_s \sin \lambda \end{aligned} \tag{26}$$

The next step is to determine whether the spacecraft is in sunlight or eclipse. This requires knowing the angle between the sun and spacecraft position vectors (in the *GCI* frame). Since the CubeSat position vector in the *GCI* frame is known, it is possible to determine the direction of the spacecraft with respect to the sun vector. The dot product of the two unit position vectors is the cosine of the angle between them.

$$\hat{\mathbf{R}}_s \bullet \hat{\mathbf{R}}_c = \cos \theta \tag{27}$$

where $\hat{\mathbf{R}}_s$ is the unit earth-sun vector (i.e. the vector), and $\hat{\mathbf{R}}_c$ is the unit CubeSat position vector (i.e. the solution of Eq.(3) divided by its magnitude). Figure 4 shows a drawing of the sun vector and spacecraft position vector in the *GCI* frame. If the dot product shown in Eq. (27) is positive (i.e. θ is less than 90°) the CubeSat will be in daylight. On the other hand, if the dot product is negative there are two possibilities, the CubeSat could be in eclipse or in daylight. Using the dot product, it is possible to decompose the spacecraft position vector, $\mathbf{R}_c$, into a component along the direction of the sun vector and a component perpendicular to it.

$$\mathbf{R}_c = \mathbf{R}_{c,s} + \mathbf{R}_{c,\perp} \tag{28}$$

Solving Eq. (28) for the perpendicular component:

$$\mathbf{R}_{c,\perp} = \mathbf{R}_c - \mathbf{R}_{c,s} \tag{29}$$

20

Assuming a cylindrical shadow model, the spacecraft will be in eclipse if the following two conditions are fulfilled:

- The angle between the earth-sun vector and the spacecraft position vector is obtuse: $\theta > 90^{\circ}$

- The CubeSat position vector component that is perpendicular to the earth sun-vector is smaller than Earth's radius: $\left\| \mathbf{R}_{c,\perp} \right\| < R_E$

The representation of the sun and spacecraft position vectors can be seen in Figure 4.
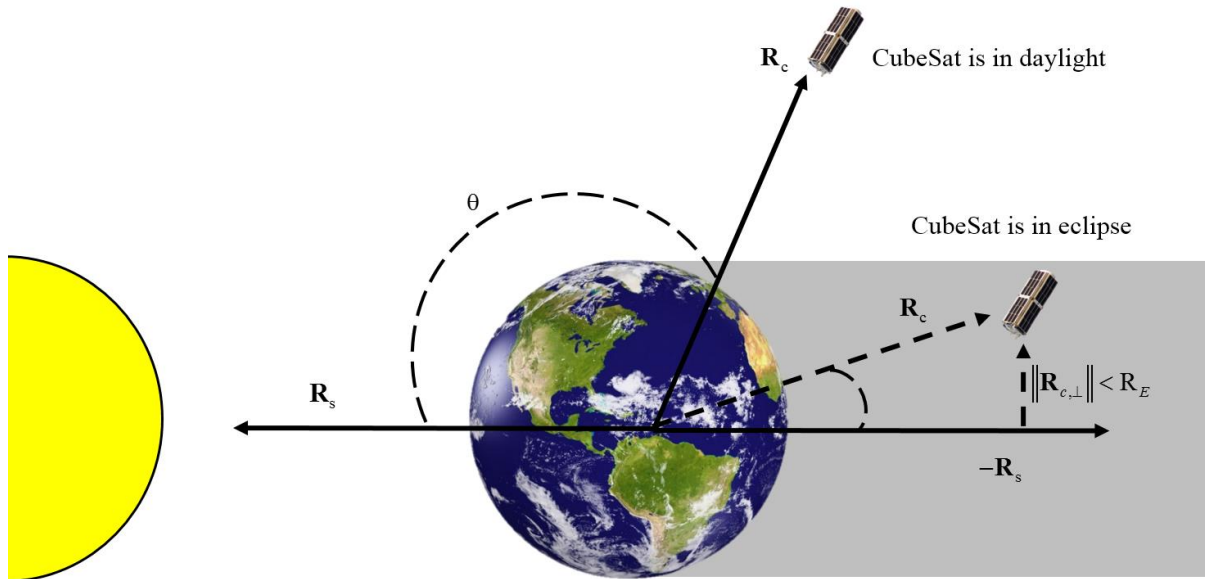
Figure 4: Daylight/eclipse definition

4.2.2. *Solar Power Calculation*

The solar power generated by the cells when the CubeSat is in daylight depends on the incident angle on the cells. The first step is to convert the earth-sun vector from the *GCI* frame to the *NTW* frame, via the transformation matrix S^{NTW}, as shown in Eq.(30).

$$\mathbf{R}_{s,NTW} = \mathbf{S}^{NTW} \begin{bmatrix} R_{s,x} \\ R_{s,y} \\ R_{s,z} \end{bmatrix} = \begin{bmatrix} \hat{N} \\ \hat{T} \\ \hat{W} \end{bmatrix}^T \begin{bmatrix} R_{s,x} \\ R_{s,y} \\ R_{s,z} \end{bmatrix} \tag{30}$$

where the components of S^{NTW} are defined as

$$\hat{N} = \frac{\dfrac{v_a}{\|v_a\|} \times \dfrac{r_a \times v_a}{\|r_a \times v_a\|}}{\left\| \dfrac{v_a}{\|v_a\|} \times \dfrac{r_a \times v_a}{\|r_a \times v_a\|} \right\|} \qquad \hat{T} = \frac{v_a}{\|v_a\|} \qquad \hat{W} = \frac{r_a \times v_a}{\|r_a \times v_a\|}$$

When the angle between the sun vector and a vector normal to the surface of a solar panel is 0°, the power generated by the cells is maximized. On the other hand, if the angle is equal or larger than 90°, there is no power generation since there are no incident solar rays on the solar panel. Therefore, the amount of power generated at a given moment depends on the cosine of the aforementioned angle. Assuming that the attitude of the CubeSat is fixed in the *NTW* frame, the angles between the spacecraft solar panels and the sun vector are defined, as seen in Figure 5.
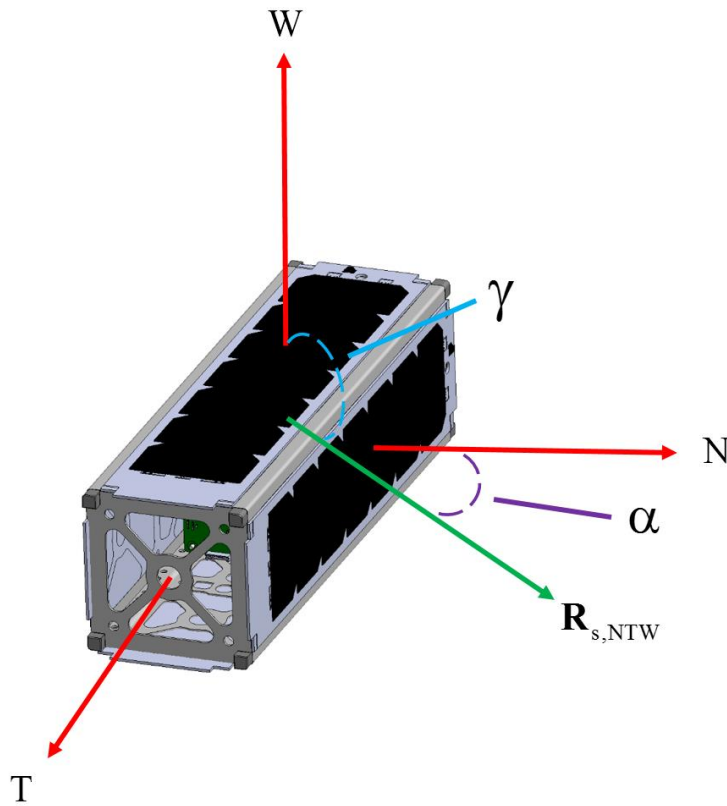
Figure 5: Solar incident angles definition

Hence the solar power equation can be written as:

$$P = I \cdot P_0 \cdot \left(\left| \cos\alpha \right| + \left| \cos\gamma \right| \right) \tag{31}$$

where I is defined as the illumination factor, equal to 0 when the CubeSat is in eclipse and 1 when the CubeSat is in daylight. P_0 is the maximum power generated by one 3U solar panel (i.e. $P_0 = 8.33W$). The absolute value of the cosines is considered because when the angle is negative the opposite side is being illuminated.

4.2.3. *Power Availability and Distribution*

The power allocated to the electric propulsion system at all times (P_{EP}) was conservatively assumed to be 2 W. This is assumed to be constant throughout the mission and well within the capability of commercially available batteries with regard to power production during eclipse. Given the drag at 210 km, failure to provide thrust would result in a loss of altitude of approximately 3 km over the first 24 hr period, and atmospheric reentry in 8.3 days. Therefore, orbit maintenance needs to occur continuously. For this reason, the power to the thrusters P_{EP} and OBC is prioritized before allotting power to the payload, battery charging, and other subsystems. The power available to all systems on the spacecraft other than the thruster is denoted as $P_{S/C}$. While a detailed power budget for a specific science mission was beyond the scope of this study, previously flown CubeSats can provide an estimate of what might be required for common bus functions. For example, on the Can-X2 mission, the average spacecraft power (excluding payload) will be approximately $P_{S/C} \sim 1.25$ W [12]. In this work, it is assumed that the power available to the spacecraft, $P_{S/C}$, which includes power for the OBC and power to charge the batteries (if in sunlight), will vary depending on the solar power available at any particular time. Any power in excess of the propulsion and OBC is used to charge the batteries to insure the thrusters and OBC can continue to operate in eclipse.

During illumination, the solar panels need to generate enough power to maintain science and bus operations $P_{S/C}$ during daylight and charge the batteries to maintain thruster and OBC operation during eclipse. The average power available for the spacecraft bus and payload during one orbital period is calculated using Eq. (32), derived from a general expression by Wertz and Larson [24], as explained in detail in Appendix A.

$$P_{S/C} = E_{SA} \left(\frac{X_e X_d}{T_e X_d + T_d X_e} \right) - P_{EP} \tag{32}$$

where E_{SA} is the energy generated by the solar arrays (in Joules). T_d and T_e are the times spent in daylight and eclipse during one orbit, respectively. X_e is the power transfer efficiency from the solar arrays through the batteries to the loads, and X_d is the power transfer efficiency from the arrays the loads. The efficiency depends on the type of power regulation: direct energy transfer or power tracking. Direct energy transfer is simple, but requires very large solar arrays; thus is deemed unsuitable for this type of mission. Maximum power point tracking (MPPT), as described by Clark and Lopez [25], is optimal for CubeSats since array power is maximized. MPPT regulation results in path inefficiencies of 5-10 %. In this study it is assumed that X_e and X_d are equal to 0.9.

Over the course of the primary mission (Phase II), the average, non-propulsive power available per orbit, $P_{S/C}$, was found to range from a minimum value of approximately 0.50 W to a maximum value of 4.25 W. Over the course of the primary mission, 87 orbits (9.31% of the time spent in eLEO) have an average bus power, $P_{S/C}$, of less than 1.0 W. These cycles of low solar power generation happen twice during the mission, the first cycle lasts for 46 orbits and the second one lasts for 41 orbital periods, with approximately 467 orbits of high solar power generation between them. As already stated, these variations are a result of both variations in the orbital elements resulting from perturbations due to the non-spherical earth, as well as the changing orientation of the spacecraft-sun vector. These results show that in the worst case, there will only be 0.50 W, in addition to the 2.0 W assumed for the thruster, available for operation

of the OBC. A typical CubeSat OBC, such as the Innovative Solutions in Space (ISIS) OBC has a nominal power consumption of 400 mW[10]. During these low power periods, the spacecraft operation will likely be limited to orbit maintenance and minimal housekeeping functions. A representation of the power generation and distribution during two illustrative orbital periods is shown in Figure 6. It can be seen that 2.0 W of power are allocated to the propulsion system, in daylight and eclipse. If the solar power generated increases, as happens during the 2nd orbit, the average power available for the spacecraft bus increases as well. The area under the power generation curve (P_{SA}) will be equal to the area under the average power consumption curves ($P_{S/C}$ and P_{EP}), with some additional area (not shown) representing losses.
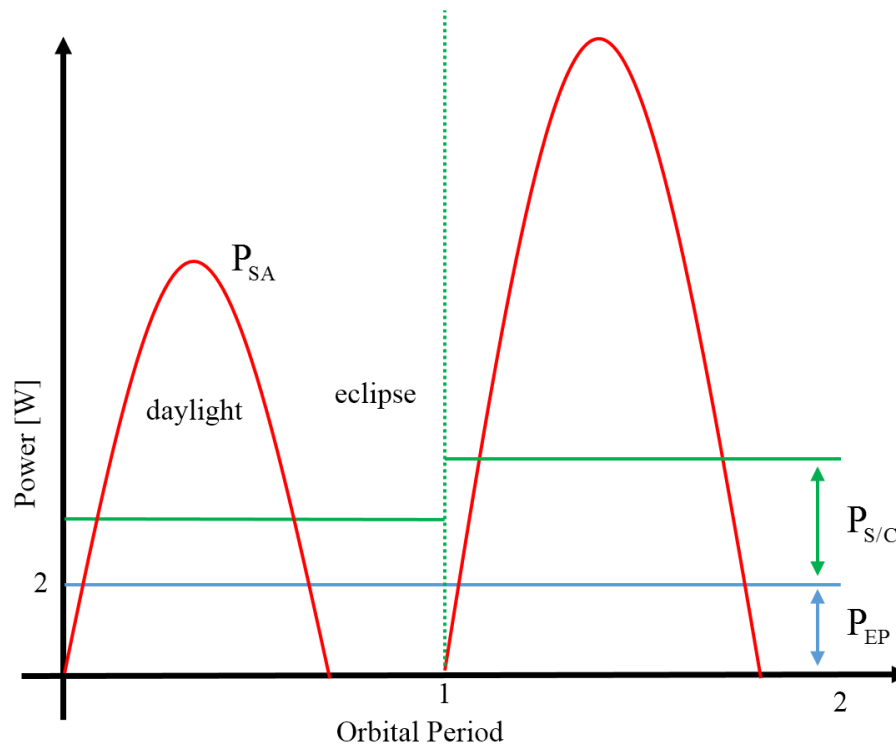
Figure 6: Power generation and distribution

4.3. Propulsion System

For the range of altitude corresponding to eLEO, where the propulsion system is continuously used to counteract (though not to cancel) drag forces, the thruster will need throttling capability. Previous authors have reviewed propulsion options available for CubeSats [9], [10]. For the purpose of this study, a baseline thruster was selected that could be accommodated within 1U of a 3U CubeSat and that could provide sufficient thrust ($0.1 - 1.0$ mN) at low power (< 5 W) to counteract the effect of drag at the altitude of interest. The actuator baseline for this work will produce thrust in the along-track direction, and consists of a single Busek Electrospray Thruster System (BET-1)[11].

The mission described in this study imposes several requirements on the propulsion system, such as a high thrust-to-power ratio, high Isp (to minimize propellant consumption), low system mass and compact dimensions to fit inside a CubeSat. Furthermore, it is desirable the thruster have the capability to modulate thrust level continuously over a range of 0.060 to 0.175 mN. As defined in Chapter 4.6, the orbit is slightly eccentric, thus the atmospheric density fluctuations caused by the spacecraft's periodic dipping into the lower atmosphere determines the throttling range of the thruster. These constraints limit the thruster choices to specific electric propulsion technologies. A brief summary and analysis on the available technologies is presented in this section.

Pulsed Plasma Thrusters (PPTs):

Pulsed plasma thrusters offer the advantages of solid propellant storage (Teflon), modularity and proven operation [9]. PPTs have been used in space since the 1960s. In fact, PPTs were the first application of electric propulsion in space, they were used in the Russian Zond 2 spacecraft in 1964 for attitude control [26]. Miniaturized PPTs, such as the micro-PPT developed by the Air Force Research Laboratory (AFRL) in 2002, can provide thrust levels of between 2 and 30 μN at power levels of between 1 and 20 W. The

---

[11] Data available online at http://www.busek.com/index_htm_files/70008500G.pdf [accessed 20 April 2015]

thruster has a mass of 0.5 kg and demonstrated 500,000 firings [26]. Based upon the developments made by AFRL, Busek has been developing micro-PPTs for CubeSats. Busek's first generation micro PPTs, the Micro Propulsion Attitude Control System (MPACS), successfully operated on the FalconSat-3 mission in 2007 [27]. The successor thruster, Busek' BmP-220 micro-pulsed plasma thruster, is currently available COTS for CubeSats and microsatellites. The BmP-200 has the following specifications[12]:

System power	1.5 W (at 1 Hz pulsing frequency) 7.5 W (1t 7 Hz pulsing frequency)
System mass	0.5 kg
System volume	330 cm^3
Impulse bit	0.02 mN-s
Isp	536 s
Total Impulse	220 N-s (40g propellant)

Table 1: BmP-220 micro-pulsed plasma thruster specifications

While there has been great progress in the development of micro-PPTs, they have low efficiencies, and their operation is inherently in a pulsed mode, which is not the best option for missions where continuous throtability is required. Because of their ability to provide very small I_{bits}, PPTs are more suitable for precision pointing and attitude control than for orbital maintenance maneuvers.

Miniature Ion Engines:

Ion engines present several advantages for CubeSat propulsion, such as high efficiency, high Isp, and the ability to modulate thrust amplitude in smooth way, as opposed to chemical and PPT alternatives. Several miniaturized ion engines have been proposed for formation flying and space telescope missions, nonetheless, these engines could be used for CubeSat applications. Mueller identifies three viable thruster alternatives: the Miniature Xenon Ion Thruster (MiXI), developed at JPL and UCLA; the µNRIT-2.5, developed at the University of Michigan; and the MRIT, developed at Pennsylvania State University.

---

[12] Data available online at http://busek.com/technologies__ppt.htm [accessed 14 June 2015]

	MiXI	µNRIT-2.5	MRIT
Thrust (mN)	0.01 – 1.5	0.05 – 0.6	0.001 – 0.06
Isp (sec)	2500 – 3200	2861	5480
Power (W)	13 – 50	13 – 34	
Electrical Efficiency (%)	>40	4 – 47	15
Mass Utilization (%)	>70	15 – 52	
Diameter (cm)	3	2.5	2
Mass (g)	200	210	
Propellant	Xenon	Xenon	Argon

Table 2: Miniature Ion Engine Performance

The MRIT and µNRIT provide thrust levels that are too low for the mission requirements, atmospheric drag in the low thermosphere is estimated to be in the order of mN, while these engines provide thrust on the µN. While the MiXI thruster does provide the necessary thrust magnitude, its thrust to power ratio is too low. The MiXI operates at a minimum power of 13 W [13]. A CubeSat with body mounted solar panels will generate an average power that is < 6 W per orbit, considerably less than the required power for micro-ion engine technology.

Miniature Hall Thrusters:

Mueller additionally identifies candidate Hall thruster technologies for microsatellites. Hall thrusters have faced considerable challenges in their miniaturization, thruster size reduction causes severe efficiency losses (see MIT thruster specifications below).

	BHT-200	SPT-30	MIT	PPPL CHT 2.6	PPPL CHT 3.0
Thrust (mN)	4 – 17	5.6 – 13	1.8	2.5 – 12	3 – 6
Isp (sec)	1200 – 1600	576 – 1370	865		1100 – 1650
Power (W)	100 – 300	99 – 258	126	50 – 300	90 – 185
Efficiency (%)	20 – 45	16 – 34	6	15 – 32	20 – 27
Mass (g)	<1	~1			
Dia (cm)	2.1	3	0.4	2.6	3
Propellant	Xenon	Xenon	Xenon	Xenon	Xenon

Table 3: Miniature Hall Thruster Performance

As can be seen in Table 3, the necessary power to operate miniature Hall thrusters is prohibitive, even more than ion engines.

Significant challenges arise in the process of miniaturizing the discharge chamber of ion and Hall thrusters, which leads to efficiency losses and higher power requirements. These technologies remain

suitable only for larger spacecraft, and have not been considered as viable options for this study. Fortunately, there are electric propulsion technologies that do not required plasma discharges to operate, such as electrospray colloid thrusters.

Electrospray Colloid Thrusters:

Colloid thrusters use ionic liquids as propellant. Charged droplets are generated by applying a strong electrostatic field and extracted to generate thrust, as shown in Figure 7. Electrospray thrusters represent a practical propulsion alternative for orbital maintenance in this niche of altitude and spacecraft power, mass, and volume. These thrusters are compact and lend themselves to scaling and miniaturization. Colloid thruster technology advanced significantly during the last decade, through the development of the thrusters for NASA's ST-7 [28] and Laser Interferometry Space Antenna (LISA) flight programs [29]. NASA and ESA selected a thruster developed by Busek and JPL for these missions. The technology leveraged from the ST-7 design is now available for use in nanosatellites [30]. The 'Busek Electrospray Thruster' (BTE – 1) has a system volume of 0.5 U and a system mass of < 1.15 kg. The thruster power consumption is < 5 W, and can deliver a maximum thrust of 1.0 mN[13]. Figure 8 shows a picture of BET – 1 and its miniature precision valve.
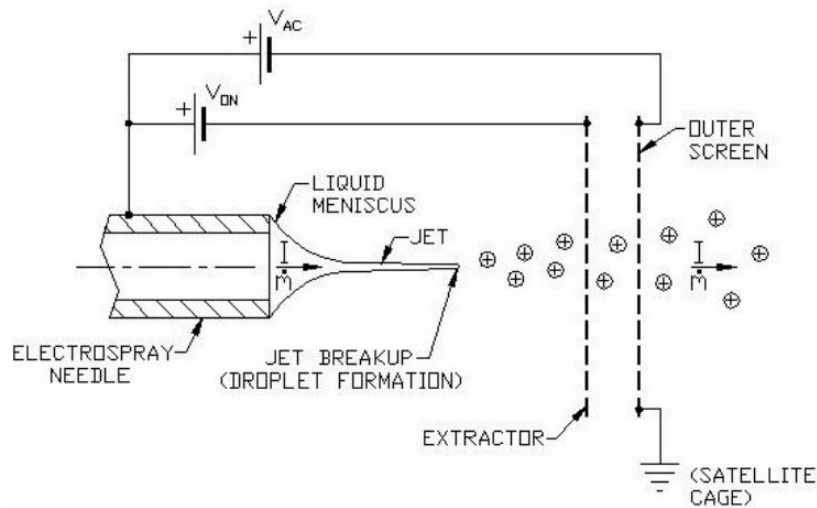
Figure 7: Schematic of electrospray thruster [30]

---

[13] Data available online at http://www.busek.com/index_htm_files/70008500G.pdf [accessed 20 April 2015]
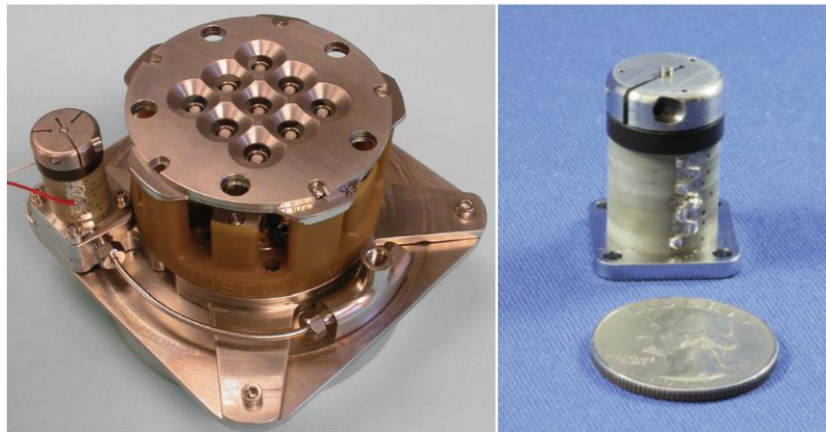
Figure 8: BET - 1 and miniature precision valve. © 2015 Busek Co. Inc. [37]

Additionally, electrospray propulsion is an attractive propulsion technology because its operation covers a wide range of specific impulse, from a few hundred to more than a thousand seconds, allowing substantial maneuverability of a CubeSat equipped with it [9]. In low Isp mode, the system would operate in high thrust-to-power for rapid maneuvering, and in high Isp mode low thrust-to-power operation allows large ΔV maneuvers. Because of the wide range of operating modes, high Isp, compact dimensions, low system mass, low power requirement, and the use of non-toxic, non-volatile propellant, the BET-1 was selected for this study.

The BET – 1 specifications for two representative operating conditions are shown in Table 4:

Power [W]	Thrust [mN]	Isp [s]
2.0	0.175	500
15.0	1.000	800

Table 4: BET – 1 specifications

The 1st operating point is an assumed, de-rated, operating point. The 2nd, high power operating mode was obtained from the data sheet available in Busek's website[14]. For the mission under study, the BET-1 would be operated in the low-power mode (i.e. the 1st operating point in table 4), at the expense of decreased Isp. The thrust uncertainty is assumed to be ± 0.2% of the commanded thrust, based on the thrust resolution reported by Spence et al for the ST7 thrusters [28] . The following expression for the along-track thrust acceleration uncertainty was used

---

[14] Data available online at http://www.busek.com/index_htm_files/70008500G.pdf [accessed 20 April 2015]

$$\varepsilon_T = \frac{(T_T)(0.002)}{m(t)}[\text{rand}(-1,1)] \tag{33}$$

where $m(t)$ is the instantanenous spacecraft mass, T_T is the commanded thrust and [rand(-1,1)] is a uniformly distributed random number between -1 and +1, bounding the uncertainty range within the $\pm\, 0.2\%$ limit. Propellant reservoirs are available in either 50 mL and 100 mL. For this study, the larger 100 mL reservoir was selected with a corresponding propellant mass of 172.02 grams.

4.4. Attitude Control

Active attitude control is required for detumbling the spacecraft after deployment from the ISS. Active attitude control can be achieved with magnetorquers, which are common COTS attitude actuators available for CubeSats. Full, three-axis control can be achieved with three magnetorquers, placed orthogonal to each other. CubeSat magnetorquers provide high magnetic moments (0.2 Am^2) for low power (200 mW)[15]. Another active option would be a reaction wheel assembly as assumed in the drag-free spacecraft investigated by Conklin et al [8].

Because the attitude control is not the focus of this work, the CubeSat in the simulation is assumed to be designed for passive attitude stability during the main mission (Phase II). Passive attitude control, or weathercock stability, is achieved by ensuring that the center of pressure of the spacecraft is behind its center of mass. NASA successfully demonstrated the feasibility of an additional type of passive aerostabilization in LEO, when the PAMS spacecraft was deployed from the Space Shuttle Endeavour in 1996. The PAMS satellite used magnetic hysteresis material for angular rate damping, and its dimensions were similar to those of a CubeSat. PAMS was designed for aerodynamic stability in altitudes from 250 to 325 km [31].

---

[15] Data available online at http://www.cubesatshop.com/index.php?option=com_virtuemart&Itemid=69 [accessed 14 May 2015].

A CAD model of the CubeSat, showing the solar panels and the propulsion system, can be seen in Figure 9:
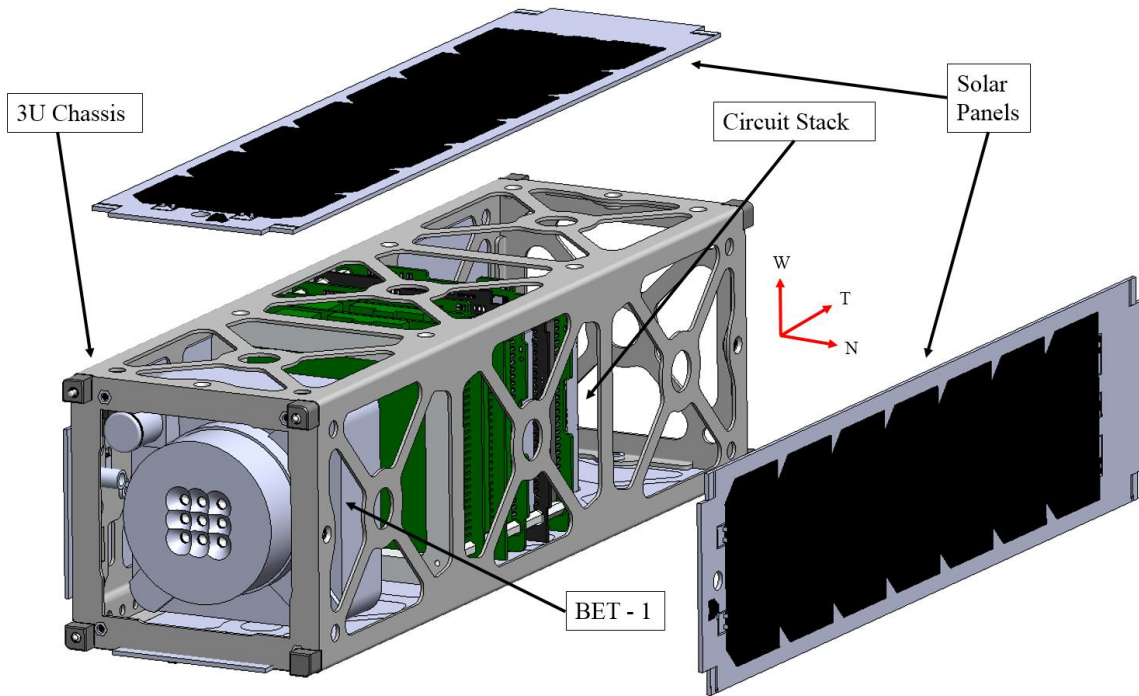
Figure 9: CubeSat bus

4.5. GPS Receiver

The measurement noise, $\boldsymbol{\varepsilon}_{GPS,k}$, and therefore the performance of the EKF and the energy-controller depend on the type of GPS receiver considered for the mission. Single-frequency (L1) receivers for space applications usually have a 2-σ uncertainty in position of 20 m and 0.25 m/s in velocity[16]. The GPS receiver assumed in the simulations for this study is the SGR-05U single-frequency receiver manufactured by Surrey Satellite Technology LLC, with a mass of 40 g and a nominal power consumption of 0.8 W. The SGR-05 has a maximum position and velocity update frequency of 1 Hz (i.e. once per second). It is worth noting that dual-frequency receivers provide a better performance, since the effects of the ionosphere on the signal

---

[16] Data available online at http://www.sst-us.com/shop/satellite-subsystems/gps/sgr-05u-space-gps-receiver [accessed 20 May 2015]

are minimized. While dual-frequency receivers have been used in space for several years, they were not small enough to be used in nanosatellites until recent progress achieved at the University of Texas. The FOTON receiver was developed at the University of Texas, fits within a 0.5U CubeSat form factor and is anticipated to have a 2-σ uncertainty in position of 2.94 m and 0.58 m/s in velocity [32]. However, due to its power requirement of 4.5 W, it was eliminated from consideration in the simulations.

4.6. Deployment and Reference Orbit

CubeSats have always flown to space as secondary payloads. The characteristics of orbital insertion depend on the requirements imposed by the primary customer. Therefore, it is unrealistic to expect that the CubeSat would be deployed directly into eLEO, since most spacecraft are placed in higher orbits in order to maximize lifetime. For the mission evaluated in this simulation, the International Space Station (ISS) is assumed to serve as the point of deployment. The space station is equipped with NanoRacks platforms, experimental external research facilities that support CubeSat operations by providing power and data capabilities, in addition to deployment [33]. Each platform provides room for up to 16 CubeSats. Several Planet Labs' CubeSats have been deployed from the NanoRacks platforms. The space station is resupplied frequently; hence there are several opportunities to deliver CubeSats to the ISS every year. The ISS is in a near-circular orbit, at a mean altitude of 414 km and an inclination of 51.64°. An eLEO orbit with the same inclination as the ISS presents the opportunity of conducting *in-situ* atmospheric measurements at a wide range of latitudes.

It is assumed that the 3U CubeSat has a wet mass of 4 kg, and a 100 mL propellant reservoir as described earlier. The simulation consists of two phases. In Phase I the CubeSat is deployed from the ISS, and the on-board propulsion system is used to decrease the altitude of the spacecraft until the target altitude is reached. As noted earlier, the "target" corresponds to a mean altitude, not a specific orbital trajectory. Because the CubeSat is originating in a near-circular, 51.64° inclination orbit, the target altitude will also correspond to a near-circular orbit with this same inclination at the end of Phase I. Once the target altitude

is attained, orbital maintenance (Phase II) starts and continues until all the propellant is consumed. The target altitude for Phase II is selected based on the maximum thrust of the propulsion system which has been assumed. If the altitude is too low the drag force will be larger than the thrust for extended periods of time, and the CubeSat could re-enter the Earth's atmosphere prematurely. Therefore, the target altitude will correspond to an orbit where the drag force magnitude at perigee is close to the maximum thrust available. For the BET-1 thruster chosen for this simulation and the atmospheric model data, it is estimated that the maximum thrust would be approximately equal to the drag at a perigee of 205 km. To be conservative, and to minimize the possibility of saturating the controller, the selected target orbit perigee was 210 km.

The orbital elements of the target orbit at the beginning of Phase II are shown in Table 5.

Argument of the perigee (ω)	76.15º
Right ascension of the ascending node (RAAN)	352.6º
True anomaly (θ)	323.7º
Inclination (i)	51.63º
Eccentricity (ε)	0.0022
Semi-major axis (a)	6603 km

Table 5: Orbital elements at start of Phase II

5. Results

5.1. Solution Strategy

The model Eqs. (1,2) have been implemented in a simulation code written in MATLAB (Mathworks Inc., Natick MA). While all the simulation performed for this work was completed in MATLAB, it is important to identify which elements would be performed on an actual spacecraft using the commercially available OBC. The simulation code integrates the two dynamic equations of motion (Eqs. 1 and 2) over an interval of one "simulation time step," hereafter referred to as just the "time step." The time step chosen for this study is 0.1 s.

The estimated spacecraft state (position and velocity) is updated and "corrected" with GPS information only when it is available, i.e. every ten time steps (corresponds to 1 second). The applied thrust, propellant consumption, instantaneous spacecraft mass, and ballistic coefficient are calculated at every time step. The results of the integration are used as the initial conditions for the next integration step. A variable order, Adams-Bashforth-Moulton integration scheme is used. This solver is suitable for computationally intensive problems, and when stringent tolerances are required[17]. A flowchart of the MATLAB simulation is shown in Figure 10. In this figure, the calculations bounded by the dashed border are used to simulate the corrupted GPS data which is available to the spacecraft OBC. The estimated state, as determined by the EKF as well as the thruster commands, are generated by the calculations bounded by the solid border. Thus, all the computations in the solid boxes will be performed in real-time on the spacecraft by the onboard computer.

---

[17] Data available online at http://www.mathworks.com/help/matlab/ref/ode113.htm [accessed 14 May 2015]

A more detailed flowchart of the algorithm and the simulation can be seen in Appendix B. As mentioned in Chapter 2, the "target" orbit is propagated in the simulation for comparing it's evolution with the one of the "actual" orbit. The "target" orbit would not be propagated in the OBC, since only the orbital energy (E_t) of the "target" orbit is necessary, and is always constant. The OBC needs to propagate one equation of motion, the "estimated" orbit. The "actual" orbit is propagated in the simulation to generate the sensors measurements, but in reality the actual (albeit corrupted) state would be obtained directly from the GPS receiver.

MATLAB Simulation

Spacecraft:
$$\ddot{\mathbf{r}}_a(t) = -\mu \frac{\mathbf{r}_a(t)}{\|\mathbf{r}_a(t)\|^3} + \mathbf{a}_{ns,a}(t) + \mathbf{a}_{d,a}(t) + \mathbf{a}_{T,a}(t)$$

r_a, v_a

$+$ ← noise

$$\mathbf{y}_{r,k} = \mathbf{r}_{a,k} + \boldsymbol{\varepsilon}_{GPS,r}$$
$$\mathbf{y}_{\mathrm{v},k} = \mathbf{v}_{a,k} + \boldsymbol{\varepsilon}_{GPS,\mathrm{v}}$$

measurements

- State estimated by the on-board computer:

$$\ddot{\mathbf{r}}_e(t) = -\mu \frac{\mathbf{r}_e(t)}{\|\mathbf{r}_e(t)\|^3} + \mathbf{a}_{ns,e}(t) + \mathbf{a}_{d,e}(t) + \mathbf{a}_{T,e}(t), \qquad t \in [t_{k-1}, t_k)$$

$k = 1 \dots$ nsteps
(-) *a priori*
(+) *a posteriori*

$\overline{K}_k$ is zero between GPS measurements

- Extended Kalman Filter:

Condition the predicted estimate on the measurement:

$$\begin{pmatrix} \mathbf{r}_{e,k} \\ \mathbf{v}_{e,k} \end{pmatrix}_{(+)} = \begin{pmatrix} \mathbf{r}_{e,k} \\ \mathbf{v}_{e,k} \end{pmatrix}_{(-)} + \overline{K}_k \left[\begin{pmatrix} \mathbf{y}_{r,k} \\ \mathbf{y}_{v,k} \end{pmatrix} - \begin{pmatrix} \mathbf{r}_{e,k} \\ \mathbf{v}_{e,k} \end{pmatrix}_{(-)} \right]$$

Solve differential matrix Riccati equation:
$$\dot{P} = F \cdot P + P \cdot F^T + G \cdot Q \cdot G^T, \quad t \in [t_{k-1}, t_k)$$
Compute the Kalman gain:
$$\overline{K}_k = P_k^- H_k^T [\mathrm{H}_k \, P_k^- H_k^T + R_k]^{-1}$$
Compute the *a posteriori* covariance matrix:
$$P_k^+ = [I_{6x6} - \overline{K}_k H_k] \mathrm{P}_k^-$$

Estimated orbital energy:
$$E_e = \frac{1}{2} v_e^2 - \frac{\mu}{r_e} \left[1 - \sum_{l=2}^{6} J_l \left(\frac{R_E}{r_e} \right)^l P_l(\sin \delta_e) \right]$$

Target orbital energy:
$$E_t = \frac{1}{2} v_t^2 - \frac{\mu}{r_t} \left[1 - \sum_{l=2}^{6} J_l \left(\frac{R_E}{r_t} \right)^l P_l(\sin \delta_t) \right]$$

Calculate energy error: $\quad \Delta E = E_t - E_e$

Calculated Thrust Accelerations
$$\mathbf{u}_e\big|_{NTW} = \left(0, \quad C \frac{T_{\max}}{m(t)} \frac{\Delta E}{\|E_t\|}, \quad 0 \right)^T$$
$$\mathbf{u}_a\big|_{NTW} = \mathbf{u}_e\big|_{NTW} + \boldsymbol{\varepsilon}_T$$

Figure 10: Simulation algorithm

Transform control accelerations to *GCI* frame:
$$\mathbf{u}_e\big|_{XYZ} = [N \rightarrow G] \mathbf{u}_e\big|_{NTW}$$
$$\mathbf{u}_a\big|_{XYZ} = [N \rightarrow G] \mathbf{u}_a\big|_{NTW}$$

5.2. Orbit Evolution

5.2.1.Phase I: Deorbit maneuver

As described in section 4.4 the CubeSat is assumed to have a minimal attitude control system for the purpose of detumbling after deployment and to point the thruster vector along the positive or negative along track direction. For Phase I, the thrust vector is oriented in the negative *T* direction in order to decrease the orbital energy and bring the spacecraft to the starting altitude for Phase II. The mass distribution on the CubeSat will be chosen to insure passive stability when in the orbit maintenance mode (Phase II). While the longitudinal axis will be rotated 180 degrees for Phase I, the drag through Phase I is minimal until the starting altitude for Phase II is approached, and any active stabilization required will be provided by the magnetorquers.

Once the spacecraft has been stabilized and oriented after deployment, a continuous thrust of 0.175 mN is applied to lower the orbital energy. The orbital transfer lasts approximately 25.21 days, or 391 orbits. Figure 11 shows the change in altitude through Phase I, with the band thickness corresponding to the spread in altitude between apogee and perigee. It can be seen that the eccentricity does not vary significantly during the maneuver.
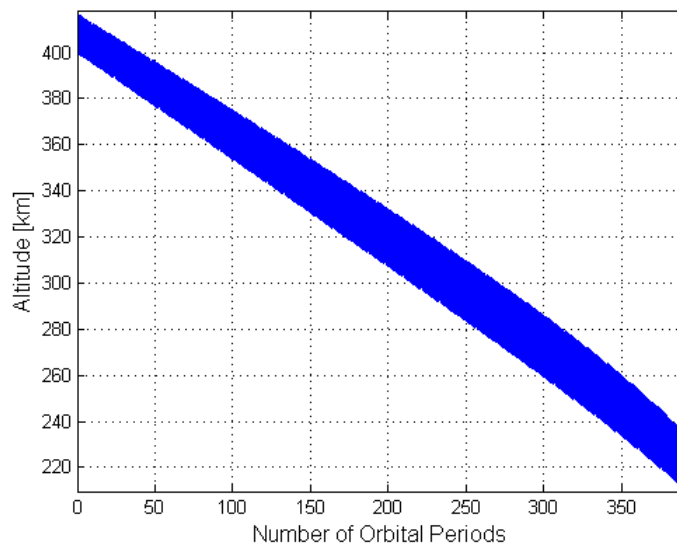
Figure 11: Phase I altitude change

The ΔV in Phase I is 96.25 m/s, and the propellant mass consumed is 77.80 grams, approximately 45.23 % of the initial propellant mass. The mass flow rate is 0.036 mg/s.

5.2.2. Phase II: Primary Mission

Once the spacecraft has reached the starting altitude for Phase II, the magnetorquers provide rotation to orient the thrust vector along the in-track direction. For the remainder of Phase II, the orientation is maintained solely through passive stability. To be conservative, it is assumed that at the beginning of Phase II the initial GPS signal has the maximum possible error based on the receiver manufacturer data: 20 m and 25 cm/s errors in position and velocity, respectively.

The primary mission lasts approximately 57.83 days, or 935.42 orbits. For clear visualization, only the first and last five orbits of the mission are shown in Figures 12-19. Figures 12 and 13 show the evolution of the spacecraft altitude.
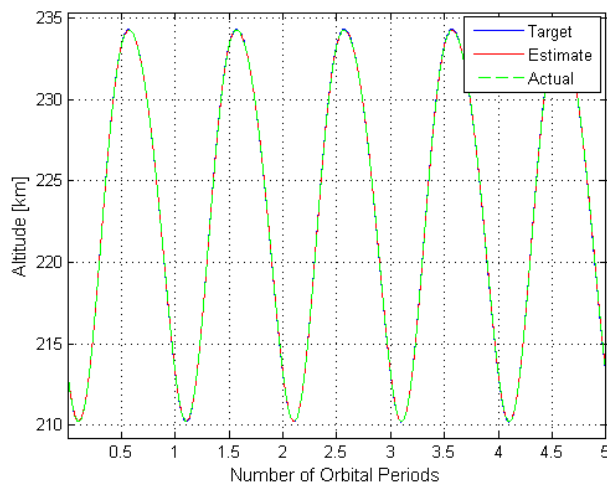
Figure 12: Initial Altitude
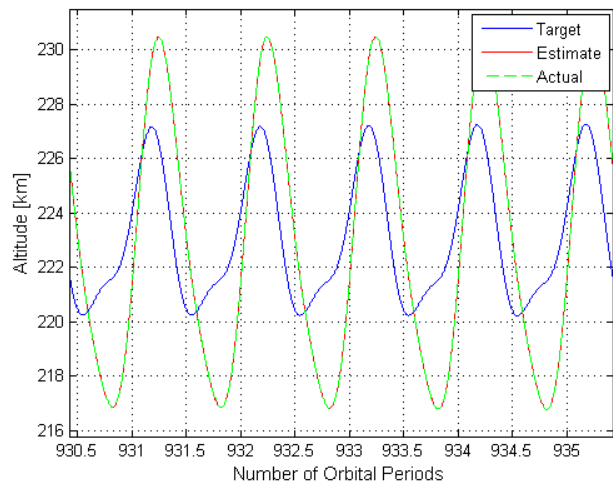
Figure 13: Final altitude

At the beginning of Phase II, the orbital altitudes corresponding to the three states are superposed. At the end of the mission there is a significant difference between the controlled and the target orbit perigee and apogee. The target state, subject to conservative gravitational forces only, has a perigee that increased by more than 10 km, and the apogee decreased by 7 km. Surprisingly, the actual orbital altitude (both max

39

and min) does not change as much as that of the target orbital altitude. The actual orbit's perigee increases by approximately 6 km, and the apogee decreases by 3 km.

The perturbations due to the non-spherical geopotential of Earth cause periodic variations in all the Keplerian orbital elements while a secular variation is a linear change in the orbital element. A short-period variation is a periodic change in the element with a period that is less than the orbital period. The dominant effects are secular variations in the right ascension of the ascending node (RAAN) and periodic variations in the inclination (i). Figure 14 shows the aforementioned dominant variations. The target and the actual orbit have a similar RAAN at the end of the mission. The nodal precession rate of the orbit is more than 5.5 degrees per day, which has a considerable effect on the solar power availability throughout the mission. The inclination of the actual orbit is 0.02 degrees lower than the inclination of the target orbit. This slight reduction in inclination is probably a consequence of atmospheric drag in the *N* and *W* directions.

Figure 15 shows the drag forces in the *NTW* frame. The along-track *T* drag force varies from 0.057 to 0.135 mN. The cross-track *W* track varies from –0.0052 to 0.0055 mN, approximately and order of magnitude less than the drag in the *T* direction. The cross-track drag is caused by the co-rotation of the Earth's atmosphere, and changes sign twice during one orbital period due to the periodic variations in latitude.
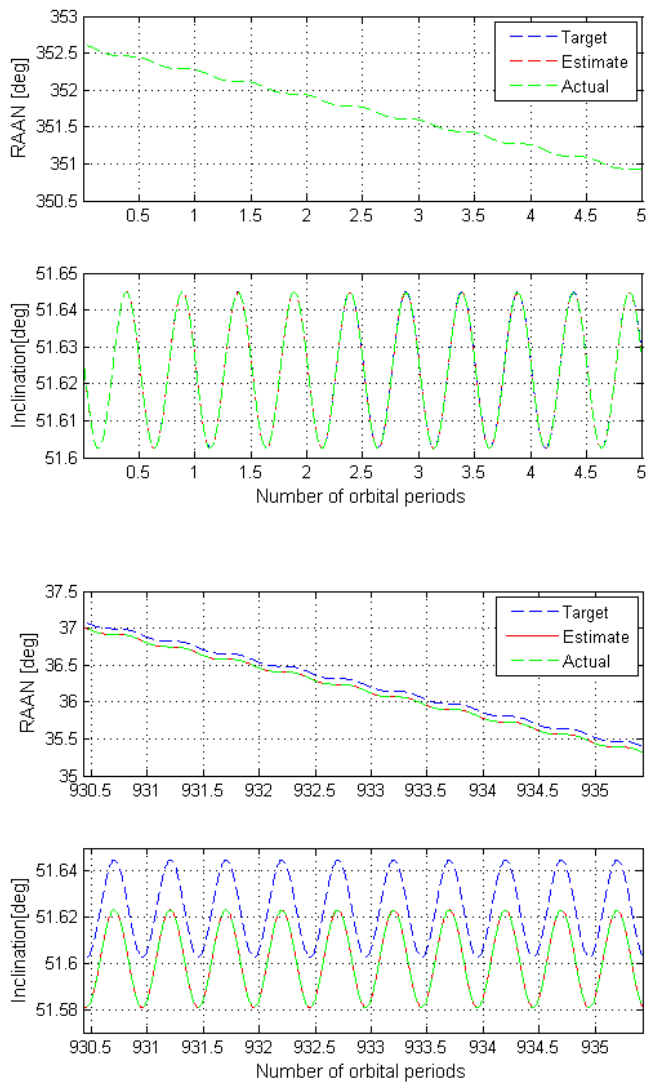
Figure 14: Orbital elements evolution
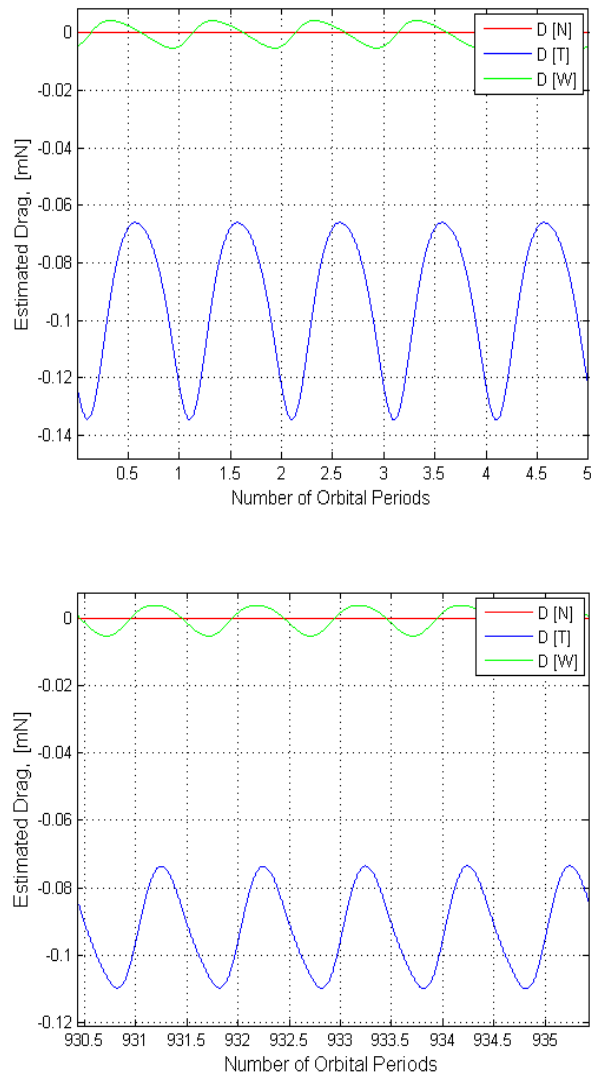
Figure 15: Drag force profile

5.3. Controller Performance

As noted in Chapter 4.3, the maximum thrust available $T_{\max}$ is 0.175 mN. However, a minimum thrust $T_{\min}$ limit has also been imposed. Due to state errors from GPS measurements, in some instances the estimated energy error will erroneously be determined to be positive. In these cases, the controller would respond as if the CubeSat is at a higher energy than the target by decreasing the thrust to zero. Toggling the thruster on and off can reduce the effective Isp considerably, since operation in this mode may lead to non-

41

optimal Taylor cone formation at the emission sites in the electrospray thruster. Therefore, instead of turning off the thruster when ΔE is positive, a minimum thrust T_{min} is applied. T_{min} has to be chosen carefully, since propellant must be conserved, and if T_{min} is too high the orbital energy would continue increasing unnecessarily.

Hence, the minimum thrust was selected to be marginally less than the force necessary to counteract the along-track T drag force at the apogee. For the orbital conditions considered, T_{min} is equal to 0.06 mN.
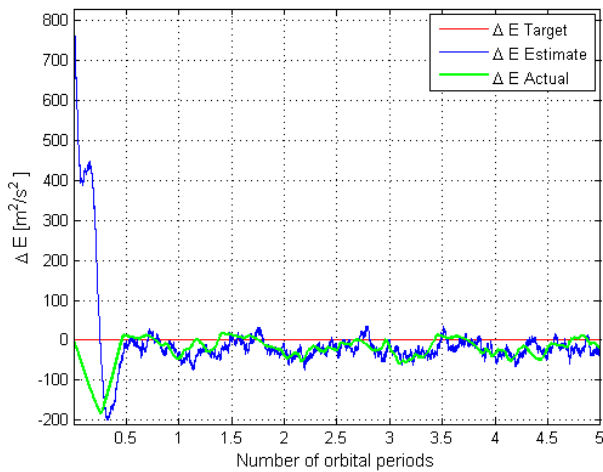
Figure 16: Energy error
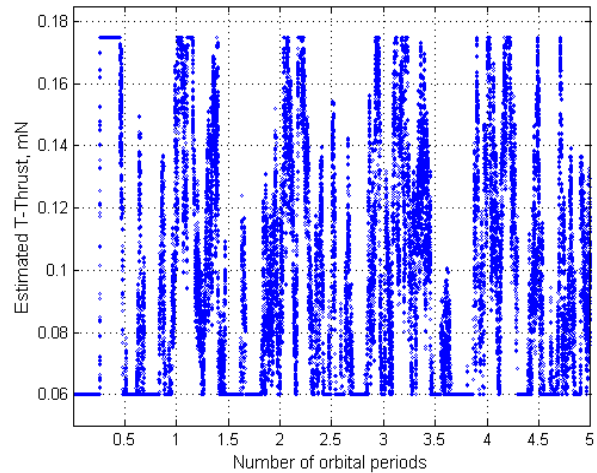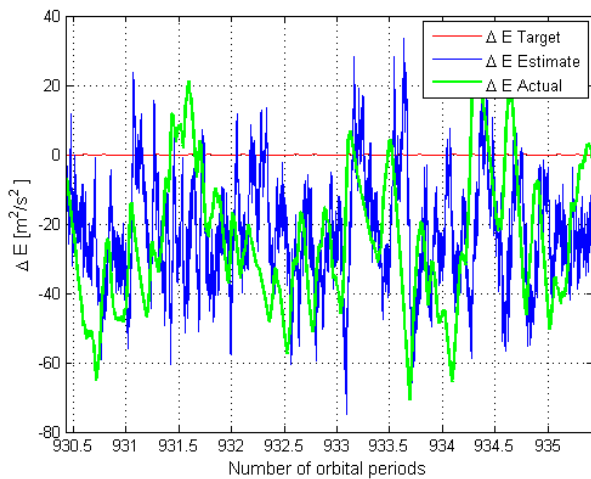
Figure 17: Estimated thrust profile

The energy error (ΔE) can be seen in Figure 16. As explained in section 4.6, the state error at the beginning of Phase II corresponds to the maximum possible, which translates to an initial estimated energy error of

823.2 m²/s². The Extended Kalman Filter reduces the error in the estimated energy and a steady state in reached after approximately half an orbital period. It is worth noting that during the first 45 minutes the thrust is set to a minimum as consequence of the estimated energy error. Therefore, the actual energy decreases until the EKF reduces the state error and the steady state is reached.

The average error of the actual orbital energy over the course of the full mission (57.83 days, or 935.42 orbits) is -19.86 m²/s², and the root-mean-square error is 25.98 m²/s². Propellant consumed when ΔE is positive is wasted. For most of the mission, the thrusters are attempting compensate for orbital energy dissipated by drag (when ΔE, is negative), while minimizing any overshoot (when ΔE, is positive), therefore, the energy error has a negative bias. The thrust profile can be seen in Figure 17. The thrust amplitude periodically varies between T_{min} and T_{max}. The maximum thruster dynamic response is approximately 1.09 µN/s, which should be well within the capability of the BET-1, which can use a combination of acceleration voltage and flow rate changes to throttle. The average mass flow rate is approximately 0.019 mg/s. The ΔV for Phase II is 119.15 m/s.

The error in the state vector is a measure of the effectiveness of the Extended Kalman Filter. Figure 18 shows the error of the magnitude of the position and velocity at the beginning of the mission. The error in position increases from 20 m to nearly 60 m during the transient before decreasing rapidly to less than 5 m, as seen in Figure 18. Figure 19 shows the errors at the end of the mission. The root-mean-square position and velocity errors are 1.19 m and 0.39 cm/s, respectively. As mentioned in Chapter 4.5, a single frequency GPS receiver has a 2-σ bound uncertainty of 20 m in position and 25 cm/s in velocity. Assuming that the noise in the GPS measurements has a Gaussian distribution, the 2-σ bound uncertainty implies that the root-mean-square measurement error in position and velocity are 12.34 m and 15.41 cm/s, respectively.

Therefore, in the steady state, the EKF successfully reduces the position error by 90.36%, and the velocity error by 97.47% relative to the maximum expected (RMS) uncertainties from the GPS.
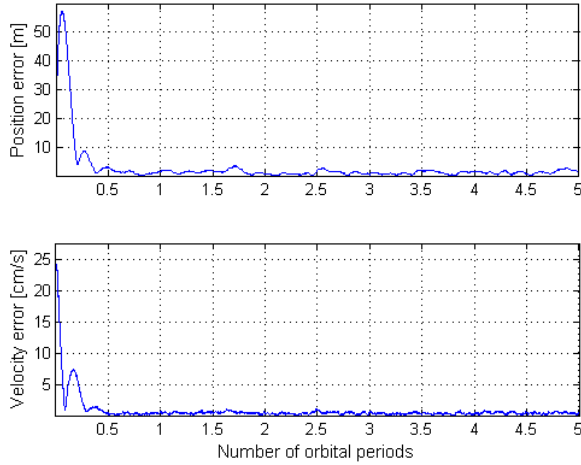
Figure 18: Initial position and velocity error
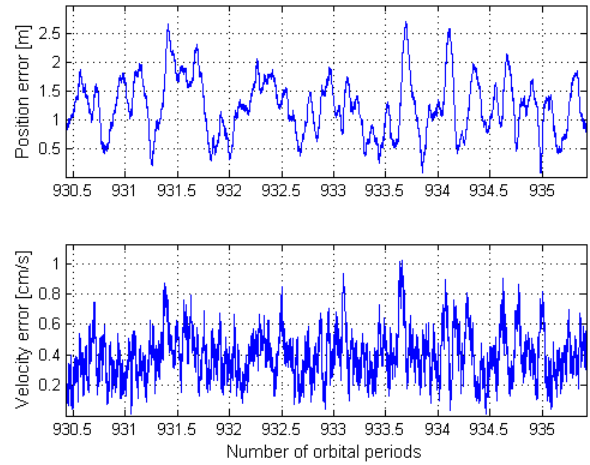
Figure 19: Final position and velocity error

6. Conclusions

A simulation of nanosatellite flight in extremely Low Earth Orbit was implemented to study the feasibility of conducting scientific missions in the lower thermosphere, an area of the atmosphere that remains virtually unexplored. The results offered in this paper suggest that a CubeSat mission in the lower thermosphere is feasible from the propulsion and control standpoint. Moreover, the mission can be accomplished with technology that is currently available, the majority (if not all) the necessary components and subsystems are COTS. For the target altitude considered and an initial propellant mass of 172.02 g, the primary mission lasts 57.83 days. If the transfer time between the ISS and the target orbit is also used to perform science, the spacecraft has a useful orbital lifetime of 83 days. The total ΔV throughout the mission is 215.4 m/s. The minimum altitude that can be attained is limited by the power available for the propulsion system. Orbital flight below 205 km would require deployable solar arrays.

Future work includes further investigation of the aerodynamic stability of a CubeSat in eLEO. Active stability methods, such as torque damping using magnetic B-dot control, and the use of miniaturized pulsed plama thrusters (PPTs) for attitude maintenance should also be considered. Innovative ways to use deployable solar arrays would enable orbital flight at altitudes between $150 - 200$ km, since the electrospray propulsion system could generate higher thrust to counteract drag in denser parts of the atmosphere. Moreover, deployable arrays can be used as fins for aerodynamic stability. Improved control systems should also be investigated to avoid the need of using a minimum thrust level (T_{min}). The present study does not consider the effect of uncertainty in the atmospheric model. Future work could include the development of a control law that uses and adaptive gain to account for such uncertainty, since the atmospheric density is not known a priori.

References

[1]   M. Williamson, "Atmospheric Skimming Satellites," *Aerospace America,* p. 9, January 2015.

[2]   C. Reigber, P. Schwintzer and H. Luhr, "The CHAMP geopotential mission," *Bollettino di Geofisica Teorica ed Applicata,* vol. 40, no. 3-4, pp. 285-289, 1999.

[3]   M. Drinkwater, R. Haagmans, D. Muzi, A. Popescu, R. Floberhagen, M. Kern and M. Fehringer, "The GOCE Gravity Mission: ESA's First Core Earth Explorer," in *Proceedings of the 3rd International GOCE User Workshop*, Frascati, Italy, 2006.

[4]   A. Jäggi, H. Bock and U. Meyer, "GOCE Precise Science Orbits for the Entire Mission," in *Proceedings of the 5th International GOCE User Workshop*, Paris, France, 2014.

[5]   P. Touboul, E. Willemenot, B. Foulon and V. Josselin, "Accelerometers for CHAMP, GRACE, and GOCE space missions: synergy and evolution," *Bollettino di Geophysica Teoretica ed Applicata,* vol. 40, no. 3-4, pp. 321-327, 1999.

[6]   M. R. Drinkwater, R. Floberghagen, R. Haagmans, D. Muzi and A. Popescu, "GOCE: ESA's First Earth Explorer Core Mission," in *Earth Gravity Field from Space - From Sensors to Earth Sciences*, Noordjwijk, The Netherlands, Springer Netherlands, 2003, pp. 419-432.

[7]   P. Marchetti, J. J. Blandino and M. Demetriou, "Electric Propulsion and Controller Design for Drag-Free Spacecraft Operation," *AIAA Journal of Spacecraft and Rockets,* vol. 45, no. 6, pp. 1303 - 1315, 2008.

[8]   J. W. Conklin, k. Balakrishnan and S. a. e. a. Buchman, "The Drag-free CubeSat," in *26th Annual AIAA/USU Conference on Small Satellites, Paper SSC12-VI-8*, Logan, Utah, 2012.

[9]   J. Mueller, R. Hofer and J. Ziemer, "Survey of Propulsion Technologies Applicable to Cubesats," in *Joint Army-Navy-NASA-Air Force (JANNAF)*, Colorado Springs, Colorado, 2010.

[10]   V. Lappas, S. Pottinger, A. Knoll, P. Shaw, D. Lamprou, T. Harle, B. Melly and M. Perren, "Micro-Electric Propulsion (EP) Solutions for Small Satellite Missions," in *2nd International Conference on Space Technology*, Athens, Greece, 2011.

[11]   J. C. Springmann, B. P. Kempke, J. W. Cutler and H. Bahcivan, "Initial Flight Results of the RAX-2 Satellite," in *AIAA/USU Conference on Small Satellites, SSC12-XI-5*, Logan, Utah, 2012.

[12]   K. Sarda, C. Grant, S. Eagleson, D. Kekez, A. Shah and R. Zee, "Canadian Advanced Nanospace Experiment 2 Orbit Operations: One Year of Pushing the Nanosatellite Performance Envelope," in *AIAA/USU Conference on Small Satellites*, Logan, 2009.

[13]   R. W. Conversano and R. E. Wirz, "Mission Capability Assessment of CubeSats Using a Miniature Ion Thruster," *Journal of Spacecraft and Rockets,* vol. 50, no. 5, pp. 1035-1046, 2013.

[14]   M. A. Viscio, N. Viola, S. Corpino, F. Stesina, S. Fineschi, F. Fumenti and C. Circi, "Interplanetary CubeSats System for Space Weather Evaluations and Technology Demonstration," *Acta Astronautica,* vol. 104, no. 2, pp. 516-525, 2014.

[15]   B. Lange, "The Drag-Free Satellite," *AIAA Journal,* vol. 2, no. 9, pp. 1590-1606, 1964.

[16]   Anonymous, "Space in Images," European Space Agency, 2015. [Online]. Available: http://www.esa.int/spaceinimages/Missions/GOCE/(class)/image?mission=GOCE&keyword=+--%253E+Keyword&idf=+--%253E+ID&Ic=on&subm3=GO. [Accessed 15 April 2015].

[17]   D. Vallado, in *Fundamentals of Astrodynamics and Applications*, El Segundo, Space Technology Library, Microcosm Press, 2001, pp. 550 - 553.

[18]   L. Blitzer, "Handbook of Orbital Perturbation," University of Arizona, 1970.

[19]   J. L. Crassidis and F. L. Markley, "Extended Kalman Filter," in *Fundamentals of Spacecraft Attitude Determination and Control*, New York, Springer, 2014, pp. 466-473.

[20]   K. Moe and M. M. Moe, "Gas-Surface Interactions and Satellite Drag Coefficients," *Planetary and Space Science,* vol. 53, no. 8, pp. 793-801, 2005.

[21] A. Hedin, "Extension of the MSIS Thermospheric Model into the Middle and Lower Atmosphere," *Journal of Geophysical Research,* vol. 96, no. A2, pp. 1159-1172, 1991.

[22] Anonymous, "3U CubeSat Side Solar Panel," Clyde Space Limited, 2015. [Online]. Available: http://www.clyde-space.com/cubesat_shop/solar_panels/3u_solar_panels/64_3u-cubesat-side-solar-panel. [Accessed 11 April 2015].

[23] Nautical Almanac Office, United States Naval Observatory, Sun, St. Louis, MO: U.S. Government Printing Office, 2011, p. C5.

[24] J. Wertz and W. Larson, Space Mission Analysis and Design, El Segundo: Microcosm Press, 1999.

[25] C. Clark and A. Lopez Mazarias, "Power System Challenges for Small Satellite Missions," in *European Small Satellite Services Symposium*, Sardinia, Italy, 2006.

[26] M. M. Micci and A. D. Ketsdever, "Pulsed Plasma Thrusters," in *Micropropulsion for Small Spacecraft*, Reston, Virginia, American Institute of Aeronautics and Astronautics, 2000, pp. 98-105.

[27] Gay, S. A. and N. A. Schmiegel, "FalconSAT-3 and the Space Environment," in *2210-182, AIAA Aerospace Sciences Meeting Including the New Horizons Forum and Aerospace Exposition*, Orlando, Florida, 2010.

[28] D. Spence, N. Demmons and T. Roy, "A Compact Low-Power High-Isp Thruster for Microsatellites," in *AIAA/USU Conference on Small Satellites*, SSC08-VII-4, Logan, Utah, 2008.

[29] J. Ziemer, M. Gamero-Castano, V. Hruby, D. Spence, N. Demmons, R. McCormick, T. Roy, C. Gasdaka, J. Young and B. Connolly, "Colloid Micro-Newton Thruster Development for the ST-7-DRS and LISA Missions," in *41st AIAA/ASME/SAE/ASEE Joint Propulsion Conference & Exhibit*, 4265, Tucson, Arizona, 2005.

[30]   T. Roy, N. Rosenblad, P. Rostler and D. Spence, "CubeSat Propulsion Using Electrospray Thrusters," in *AIAA/USU Conference on Small Satellites*, SSC09-II-6, Logan, Utah, 2009.

[31]   S. Rawashdeh, "CubeSat Aerodynamic Stability at ISS Altitude and Inclination," in *AIAA/USU Conference on Small Satellites*, SSC12-VIII-6, Logan, Utah, 2012.

[32]   A. Joplin, "Development and Testing of a Miniaturized, Dual-Frequency, Software-Defined GPS Receiver for Space Applications," Master's Thesis, Aerospace Engineering Department, University of Texas, Austin, Texas, 2011.

[33]   L. J. James E., D. M. Erb, T. S. Clements, J. T. Rexroat and M. D. Johnson, "The CubeLab Standard for Improved Access to the International Space Station," in *IEEE Aerospace Conference*, 1689, Big Sky, Montana, 2011.

[34]   P. Marchetti, J. J. Blandino and M. Demetriou, "Electric Propulsion and Controller Design for Drag-Free Spacecraft Operation," *Journal of Spacecraft and Rockets,* vol. 45, no. 6, pp. 1303 - 1315, 2008.

[35]   K. Moe and M. M. Moe, "Gas-Surface Interactions and Satellite Drag Coefficients," *Planetary and Space Science,* vol. 53, pp. 793-801, 2005.

[36]   L. J. JE, D. Erb, T. Clements, J. Rexroat and M. Johnson, "The CubeLab Standard for Improved Access to the International Space Station," in *IEEE Aerospace Conference*, Big Sky, Montana, 2011.

[37]   Busek Co. Inc., "Busek Electrospray Thrusters," 2015. [Online]. Available: http://www.busek.com/index_htm_files/70008500G.pdf. [Accessed 15 April 2015].

Appendix A: Power availability and distribution

The solar power generated during daylight for one orbital period is defined in SMAD [24], as shown in Eq. (A.1).

$$P_{SA} = \frac{\left(\dfrac{P_e T_e}{X_e} + \dfrac{P_d T_d}{X_d} \right)}{T_d} \tag{A.1}$$

Since the loads are the same throughout one orbital period, P_e and P_d are equal.

$$\begin{aligned} P_e &= P_{S/C} + P_{EP} \\ P_d &= P_{S/C} + P_{EP} \end{aligned} \tag{A.2}$$

Hence, it is possible to rewrite Eq. (A.1) in the following way:

$$P_{SA} = \left(\frac{T_e X_d + T_d X_e}{X_e X_d T_d} \right) \left(P_{S/C} + P_{EP} \right) \tag{A.3}$$

In order to obtain the energy generated by the solar arrays, Eq. (A.3) is integrated from zero to T_d.

$$\int_0^{T_d} P_{SA} \cdot dt = \int_0^{T_d} \left(\frac{T_e X_d + T_d X_e}{X_e X_d T_d} \right) \left(P_{S/C} + P_{EP} \right) \cdot dt \tag{A.4}$$

$$E_{SA} = \left(\frac{T_e X_d + T_d X_e}{X_e X_d T_d} \right) \left(P_{S/C} + P_{EP} \right) T_d \tag{A.5}$$

The energy (in Joules) generated by the solar arrays during one orbital period is E_{SA}. E_{SA}, T_e and T_d are known from the simulation. The only unknown in Eq. (A.5) is the power available for the spacecraft, $P_{S/C}$.

$$P_{S/C} = E_{SA} \left(\frac{X_e X_d}{T_e X_d + T_d X_e} \right) - P_{EP} \tag{A.5}$$

Appendix B: *Controller Design* Script User's Manual

B.1 Introduction

The code described in this file propagates the orbit of a spacecraft. For a full description of the problem addressed in this simulation, the reader is referred to the M.S thesis by Nicolas Martinez (WPI, 2015). The equation of motion includes the two-body gravitational force, J2-J6 non-spherical geopotential perturbations, atmospheric drag, and thrust forces. The main code is called "orbital_propagatorV9", which calls several subroutines to propagate the spacecraft motion. This User's Manual is organized as Follows. The main code and the subroutines are described in Section 2. This description of the subroutines is referenced to a detailed flowchart which includes the relevant equations used in the simulation. Section 3 provides a comprehensive table listing all variables used in the simulation, a list what subroutine(s) the variable is used in, and a brief description. Section 4 provides a complete list of parameters used for the reference case presented in the Thesis. The main code and all subroutines were written and solved in MATLAB.

B.2 Description of Main Code and Subroutines

Orbital_propagatorV9

The code takes the orbital and spacecraft parameters to generate a 6x1 initial state in an Earth centered inertial frame (position and velocity). It is worth noting that three states are propagated in this code: the *target*, *estimated*, and *actual* state. Hence, the array that is integrated by the ODE solver has dimensions of 18x1.

 Afterwards, the GPS noise is defined as Gaussian white noise. The orbital period, the number of periods that will be propagated and the integration time step are defined. All the variables that will be stored in arrays must be initialized as zeros, otherwise the running time increases considerably. A while-loop is started after the initial conditions have been set. There are two stopping conditions in the while-loop, the loop execution terminates when either condition is met. The 1st condition is atmospheric reentry, if the

51

spacecraft reaches an altitude of 120 km the solution is terminated. The 2nd condition is the number of time steps, once the last time step is reached the solution is terminated.

When the while-loop starts, noise is added to the *estimated* state. The *estimated* state is passed through the Extended Kalman Filter if there is a GPS update (i.e. only every 10 time steps), otherwise there is no correction (i.e. naïve observer). The next step is to generate the control signal. Finally, the second order differential equations are integrated with the MATLAB ODE solver, ode113. The equations are integrated over an interval between t_{k-1} and t_k. Only the last value of the integration is stored and used as the initial conditions for the next integration. The thrust acceleration is converted from the NTW to the ECI frame, and the propellant mass consumption is calculated. The results are stored in arrays and the spacecraft mass is updated before the next loop starts. Plots are created and results are displayed. A flowchart depicting the simulation is shown in Figure 1.

Simulation input:

- Central body parameters
- Initial state errors
- Spacecraft parameters
- GPS noise covariance
- Control parameters
- Thruster parameters
- End time and time step size

The input is provided at the beginning of the script.

Simulation output:

Plots:

- Drag forces vs time
- Altitude vs time
- Velocity vs time
- Estimated thrust vs time
- Actual thrust vs time
- State errors vs time
- Orbital element evolution vs time
- Orbital energy error vs time
- Solar power vs time

Displayed in the command window:

- Maximum and minimum drag forces
- Number of orbital periods that were propagated
- Days in orbit
- Total ΔV
- Total propellant mass consumption
- Remaining propellant mass in the tank

The flowchart shown in Figure B1 lists the name of the sub-routines in the lower right corners of the

boxes. If no name appears, the calculations are done in the main script.

INPUT

Altitude range, step size, dates, S/C size, bus mass, propellant mass, etc.

MSIS-E90 Model =>

[alt], [dens] vector

INPUT

Orbital element set (a_0, e_0, i_0, Ω_0, ω_0, v_0)
Control parameters (C)

Calculate at $t = 0$ from orbital element set

$\mathbf{r}_t ; \mathbf{v}_t$ $\mathbf{r}_e ; \mathbf{v}_e$ $\mathbf{r}_a ; \mathbf{v}_a$

Solve equations of motion with MATLAB ode 113:

$$\ddot{\mathbf{r}}_t(t) = -\mu \cdot \frac{\mathbf{r}_t(t)}{\left\|\mathbf{r}_t(t)\right\|^3} + \mathbf{a}_{ns,t}(t)$$

$$\ddot{\mathbf{r}}_e(t) = -\mu \frac{\mathbf{r}_e(t)}{\left\|\mathbf{r}_e(t)\right\|^3} + \mathbf{a}_{ns,e}(t) + \mathbf{a}_{d,e}(t) + \mathbf{a}_{T,e}(t)$$

$$\ddot{\mathbf{r}}_a(t) = -\mu \frac{\mathbf{r}_a(t)}{\left\|\mathbf{r}_a(t)\right\|^3} + \mathbf{a}_{ns,a}(t) + \mathbf{a}_{d,a}(t) + \mathbf{a}_{T,a}(t)$$

SR: V_prop12

Transform control accelerations to GCI frame:
$$\mathbf{u}_e\big|_{XYZ} = \left[N \to G\right]\mathbf{u}_e\big|_{NTW}$$
$$\mathbf{u}_a\big|_{XYZ} = \left[N \to G\right]\mathbf{u}_a\big|_{NTW}$$

Define errors

GPS update?

Yes

No

Measured S/C position and velocity:

$$\mathbf{y}_{r,k} = \mathbf{r}_{a,k} + \boldsymbol{\varepsilon}_{GPS,r}$$

$$\mathbf{y}_{v,k} = \mathbf{v}_{a,k} + \boldsymbol{\varepsilon}_{GPS,v}$$

Improve estimate based on the measurement:

$$\mathbf{x}_{e,k}^+ = \mathbf{x}_{e,k}^- + \bar{K}_k[\mathbf{y}_k - \mathbf{x}_{e,k}^-]$$

Solve differential matrix Riccati equation:

$$\dot{P} = F \cdot P + P \cdot F^T + G \cdot Q \cdot G^T$$

Compute the Kalman gain:

$$\bar{K}_k = P_k^- H_k^T [H_k P_k^- H_k^T + R_k]^{-1}$$

Compute the *a posteriori* covariance matrix:

$$P_k^+ = [I_{6x6} - \bar{K}_k H_k] P_k^-$$

SR: Kalman V2

Calculate two –body acceleration

$$\mathbf{a}_{g,t}(\mathbf{r}_t(t)) \;;\;\; \mathbf{a}_{g,e}(\mathbf{r}_e(t))$$

$$\mathbf{a}_{g,a}(\mathbf{r}_a(t))$$

Naïve observer, predicted position and velocity: $\mathbf{x}_e = \begin{pmatrix} \mathbf{r}_e & \mathbf{v}_e \end{pmatrix}^T$

Calculate J2 – J6 non-spherical effects:

$$\mathbf{a}_{ns,t}(\mathbf{r}_t(t)) \;;\;\; \mathbf{a}_{ns,e}(\mathbf{r}_e(t))$$

$$\mathbf{a}_{ns,a}(\mathbf{r}_a(t))$$

Calculate control accelerations:

$$\mathbf{u}_e\big|_{NTW} = \left(0, \quad C \frac{T_{max}}{m(t)} \frac{\Delta E}{\|E_t\|}, \quad 0\right)^T$$

$$\mathbf{u}_a\big|_{NTW} = \mathbf{u}_e\big|_{NTW} + \boldsymbol{\varepsilon}_T$$ SR: getcontrolV8

Calculate drag acceleration using MSIS-90 model:

$$\mathbf{a}_{d,e}(\mathbf{r}_e(t), \mathbf{v}_e(t))$$

$$\mathbf{a}_{d,a}(\mathbf{r}_a(t), \mathbf{v}_a(t))$$

Calculate thrust in the NTW (S/C) frame; determine thruster performance, propellant consumption and ΔV.

Propagation complete?

Plotting and results

Figure B1: Simulation flowchart

Subroutines in orbital_propagatorV9

Name	Description	Called by	Routines (it calls)	Input	Output
oe2rv	Finds state vector in ECI frame from Keplerian orbital element set			Keplerian orbital element set	State vector
quickntw	Calculates transformation matrix to convert vector from ECI to NTW frame			Vector in ECI frame	Transformation matrix
Kalman_V2	Reduces uncertainty from noisy GPS state measurements		riccatiV2	Estimated state, orbital parameter (μ), Earth's radius, GPS noise covariance	*a posteriori* estimated state
riccatiV2	Solves the differential matrix Riccati equation	Kalman_V2		State matrix (F), initial conditions from previous time step (P_k^-)	a posteriori covariance matrix (P_k^+)
sunvector	Calculates the earth-sun vector in the ECI frame			Time step (i), estimated position, Earth's radius	Earth-sun vector, Illumination factor (I)
sunpower	Calculates instantaneous power (W) generated by solar arrays			Unit earth-sun vector, illumination factor (I)	Solar power
GetcontrolV8	Calculates estimated and actual thrust to maintain target orbital energy		getdragMSIS	Estimated state, target energy	Estimated thrust, actual thrust
getdragMSIS	Finds atmospheric drag acceleration in NTW frame	GetcontrolV8		Position vector, velocity vector relative to co-rotating atmosphere, air density from look-up table	Atmospheric drag acceleration
GetsimparamV4	Extract atmospheric			Look-up table 'MSIS90_1.dat'	Atmospheric density data

	density data from look-up table				
V_prop12	Defines the three equations of motion (target, estimated and actual) that are subsequently integrated with ode113. Accelerations include two-body, J2-J6 perturbations, atmospheric drag and thrust			Initial conditions (18x1 array)	2nd order, non-linear, ordinary differential equation of motion
Coe_from_sv	Calculates the 6 Keplerian orbital elements from the state in the ECI frame			State vector, orbital parameter (μ)	Keplerian orbital elements

B3. Description of Variables used in Main Code

Variable	Subroutine(s) in which used	Units	Comment
J2J6	V_prop12		If set to 1, J_2-J_6 perturbations are activated.
mu	Kalman_V2 Getcontrol_V8 V_prop12	km^3/s^2	Earth's orbital parameter (μ)
Re	Kalman_V2 Getcontrol_V8 V_prop12 oe2rv	km	Earth's equatorial radius
W	V_prop12	rad/s	Angular speed of Earth's rotation
g		m/s^2	Earth's gravity
Cd			Drag coefficient
Ac		m^2	Cross-sectional area
Mprop0		kg	Initial propellant mass
Mdry		kg	Dry mass
M	Getcontrol_V8	kg	Wet mass
BC	getdragMSIS	kg/m^2	Ballistic coefficient
e0			Initial eccentricity
a0			Initial semi-major axis
i0			Initial inclination

Om0			Initial RAAN
om0			Initial argument of perigee
nu0			Initial true anomaly
oe			Initial orbital element set (1x6 array)
P		s	Orbital period
e_r		km	Root-mean-square position error
e_v		km/s	Root-mean-square velocity error
poserr		km	Initial position error
velerr		km/s	Initial velocity error
avg			Mean error of Gaussian white noise to model GPS uncertainty
SIGMA_r		km	Standard deviation of position noise
SIGMA_v		km/s	Standard deviation of velocity noise
Q_e	Kalman_V2		Time step delay for GPS state update
g_e	Kalman_V2		Counter for GPS update
Isp_Busek		s	Specific impulse of propulsion system
R	Kalman_V2		Covariance matrix of sensor (GPS) noise
no			Number of orbital periods that will be propagated
ENDTIME		s	Total propagation time
tstep		s	Global time step
r0		km	Initial position vector
v0		Km/s	Initial velocity vector
x1		km; km/s	Target orbit state vector
x2		km; km/s	Estimated orbit state vector
x3		km; km/s	Actual orbit state vector
j2,j3,j4,j5,j6	Kalman_V2 Getcontrol_V8 V_prop12		Constant coefficients of the spherical harmonics
rmag_0		km	Magnitude of initial position vector
vmag_0		Km/s	Magnitude of initial velocity vector
d_0		rad	Initial declination (latitude)
KE_0		J	Initial kinetic energy
PE_0		J	Initial potential energy
E_0	Getcontrol_V8	J	Initial (total) mechanical energy
alt	getdragMSIS V_prop12	km	Look-up altitude table
dens	getdragMSIS V_prop12	kg/m^3	Look-up atmospheric density table
nsteps			Total number of time steps in simulation
x		km; km/s	Initial state vector (18x1)
y		km; km/s	State vector array storage
i			Current time step
xc	quickntw	km; km/s	State vector (18x1) initial conditions for next integration
Sntw_e	Solarpower Getcontrol_V8		Transformation matrix (ECI to NTW) of estimated state

Sntw_a	Solarpower Getcontrol_V8		Transformation matrix (ECI to NTW) of actual state
tl	Kalman_V2	s	Left integration limit
tr	Kalman_V2	s	Right integration limit
tspan		s	Integration interval
r_noise		km	Instantaneous position noise
v_noise		km/s	Instantaneous velocity noise
Zr	Kalman_V2	km	GPS position measurement
Zv	Kalman_V2	km/s	GPS velocity measurement
xe		km, km/s	*A posteriori* estimated state
R_E	Sunvector Getcontrol_V8	km	Estimated position vector at i[th] step
V_E	Getcontrol_V8	km/s	Estimated velocity vector at i[th] step
Rs		km	Sun vector
Rs_hat	solarpower	km	Unit sun vector
I	solarpower		Illumination factor, 1 or 0
SPW		W	Instantaneous solar power generated
Ue	V_prop12	km/s^2	Estimated thrust acceleration
Ua	V_prop12	km/s^2	Actual thrust acceleration
xt		km, km/s	Solution of differential equation solver
AD	V_prop12	km/s^2	Estimated drag acceleration
AD3	V_prop12	km/s^2	Actual drag acceleration
scvel_t		km/s	Target velocity
scvel_e		km/s	Estimated velocity
scvel_a		km/s	Actual velocity
Tt		μN	Estimated thrust along T direction
Tt_a		μN	Actual thrust along T direction
dntw		N	Estimated drag force vector in NTW frame
dntw_a		N	Actual drag force vector in NTW frame
OE_t			Target orbital element set
OE_e			Estimated orbital element set
OE_a			Actual orbital element set
d_t		rad	Target orbit declination (latitude)
KE_t		J	Target orbit kinetic energy
PE_t		J	Target orbit potential energy
E_t		J	Target orbit mechanical energy
d_e		rad	Estimated orbit declination (latitude)
KE_e		J	Estimated orbit kinetic energy
PE_e		J	Estimated orbit potential energy
E_e		J	Estimated orbit mechanical energy
d_a		rad	Actual orbit declination (latitude)
KE_a		J	Actual orbit kinetic energy
PE_a		J	Actual orbit potential energy
E_a		J	Actual orbit mechanical energy
m		kg	Instantaneous spacecraft mass
Mprop		g	Instantaneous propellant mass
Mdot		g/s	Propellant mass flow rate

		m/s	ΔV
dvt		m/s	ΔV
j			Orbit counter for solar power calculation
Xe			Efficiency of path from solar array to batteries to loads
Xd			Efficiency of path from solar array to loads
Ts			Fraction of orbital time spent in daylight
E_sa		J	Photovoltaic energy generated in one orbital period
Td		s	Time spent in daylight in one orbit
Te		s	Time spent in eclipse in one orbit
P_ep		W	Power allocated to electric propulsion system
P_sc		W	Power allocated to spacecraft bus and payload

B4. Description of variables used only in subroutines

Variable	Subroutine(s) in which used	Units	Comment
H	KalmanV2		Jacobian of measurement model
q_v	KalmanV2	km/s	RMS of velocity in model process noise
q_a	KalmanV2	km/s^2	RMS of acceleration in model process noise
Sigma1	KalmanV2	km/s	Standard deviation of velocity in model process noise
Sigma1	KalmanV2	km/s^2	Standard deviation of acceleration in model process noise
Q	KalmanV2		Covariance matrix of model process noise
ax	KalmanV2	km/s^2	Acceleration in X direction due to central force and J2 perturbation
Agx_rx	KalmanV2		Partial derivative of two-body & J2 acceleration along X with respect to X
Agx_ry	KalmanV2		Partial derivative of two-body & J2 acceleration along X with respect to Y
Agx_rz	KalmanV2		Partial derivative of two-body & J2 acceleration along X with respect to Z
Agy_rx	KalmanV2		Partial derivative of two-body & J2 acceleration along Y with respect to X
Agy_ry	KalmanV2		Partial derivative of two-body & J2 acceleration along Y with respect to Y
Agy_rz	KalmanV2		Partial derivative of two-body & J2 acceleration along Y with respect to Z
Agz_rx	KalmanV2		Partial derivative of two-body & J2 acceleration along Z with respect to X
Agz_ry	KalmanV2		Partial derivative of two-body & J2 acceleration along Z with respect to Y
Agz_rz	KalmanV2		Partial derivative of two-body & J2 acceleration along Z with respect to Z
Ax_rx_3	KalmanV2		Partial derivative of J3 acceleration along X with respect to X

Ax_ry_3	KalmanV2		Partial derivative of J3 acceleration along X with respect to Y
Ax_rz_3	KalmanV2		Partial derivative of J3 acceleration along X with respect to Z
Ay_rx_3	KalmanV2		Partial derivative of J3 acceleration along Y with respect to X
Ay_ry_3	KalmanV2		Partial derivative of J3 acceleration along Y with respect to Y
Ay_rz_3	KalmanV2		Partial derivative of J3 acceleration along Y with respect to Z
Az_rx_3	KalmanV2		Partial derivative of J3 acceleration along Z with respect to X
Az_ry_3	KalmanV2		Partial derivative of J3 acceleration along Z with respect to Y
Az_rz_3	KalmanV2		Partial derivative of J3 acceleration along Z with respect to Z
Pk	KalmanV2		Covariance matrix
K	KalmanV2		Kalman gain
F	KalmanV2		State matrix
t1	KalmanV2		Left integration limit of differential matrix Riccati equation
t2	KalmanV2		Right integration limit of differential matrix Riccati equation
e	sunvector	degrees	Obliquity of ecliptic of the sun
Rs_mag_AU	sunvector	AU	Distance of Sun from Earth
AU	sunvector	km	1 AU in km
Rs_mag	sunvector	km	Distance of Sun from Earth in km
Rsx	sunvector	km	X coordinate of Sun's position
Rsy	sunvector	km	Y coordinate of Sun's position
Rsz	sunvector	km	Z coordinate of Sun's position
C	sunvector		Dot product between S/C position vector and
alfa	sunvector	radians	Angle between S/C position vector and the negative of the sun vector direction
R_rd	sunvector	km	S/C position component along cylindrical (shadow) radial direction
P0_s	solarpower	W	Nominal power generated by side solar panel
Rs_ntw	solarpower	W	Unit Earth-Sun vector in NTW frame
cos_alfa	solarpower		Projection of Rs_ntw in the N direction
cos_gamma	solarpower		Projection of Rs_ntw in the W direction
Sijk_e	GetcontrolV8		Transformation matrix from NTW to ECI frame for estimated vectors
Sijk_a	GetcontrolV8		Transformation matrix from NTW to ECI frame for actual vectors
C	GetcontrolV8		Controller gain
Tmax	GetcontrolV8	N	Maximum thrust
Tmin	GetcontrolV8	N	Minimum thrust
u_n	GetcontrolV8	km/s^2	Thrust acceleration along N
u_t	GetcontrolV8	km/s^2	Thrust acceleration along T
u_w	GetcontrolV8	km/s^2	Thrust acceleration along W
u_ntw_e	GetcontrolV8	km/s^2	Estimated thrust vector in NTW frame

u_ntw_e	GetcontrolV 8	km/s^2	Actual thrust vector in NTW frame
U_e	GetcontrolV 8	km/s^2	Estimated thrust vector in ECI frame
U_a	GetcontrolV 8	km/s^2	Actual thrust vector in ECI frame
r1	V_prop12	km	Target orbit position vector
v1	V_prop12	km/s	Target orbit velocity vector
rmag1	V_prop12	km	Target orbit position vector magnitude
r2	V_prop12	km	Estimated orbit position vector
v2	V_prop12	km/s	Estimated orbit velocity vector
rmag2	V_prop12	km	Estimated orbit position vector magnitude
r3	V_prop12	km	Actual orbit position vector
v3	V_prop12	km/s	Actual orbit velocity vector
rmag3	V_prop12	km	Actual orbit position vector magnitude
G1	V_prop12	km/s^2	Two-body acceleration of target orbit
G2	V_prop12	km/s^2	Two-body acceleration of estimate orbit
G3	V_prop12	km/s^2	Two-body acceleration of actual orbit
aj2_1	V_prop12	km/s^2	J2 acceleration vector of target orbit
aj3_1	V_prop12	km/s^2	J3 acceleration vector of target orbit
aj4_1	V_prop12	km/s^2	J4 acceleration vector of target orbit
aj5_1	V_prop12	km/s^2	J5 acceleration vector of target orbit
aj6_1	V_prop12	km/s^2	J6 acceleration vector of target orbit
aj2_2	V_prop12	km/s^2	J2 acceleration vector of estimated orbit
aj3_2	V_prop12	km/s^2	J3 acceleration vector of estimated orbit
aj4_2	V_prop12	km/s^2	J4 acceleration vector of estimated orbit
aj5_2	V_prop12	km/s^2	J5 acceleration vector of estimated orbit
aj6_2	V_prop12	km/s^2	J6 acceleration vector of estimated orbit
aj2_3	V_prop12	km/s^2	J2 acceleration vector of actual orbit
aj3_3	V_prop12	km/s^2	J3 acceleration vector of actual orbit
aj4_3	V_prop12	km/s^2	J4 acceleration vector of actual orbit
aj5_3	V_prop12	km/s^2	J5 acceleration vector of actual orbit
aj6_3	V_prop12	km/s^2	J6 acceleration vector of actual orbit
a,b,c,d	V_prop12		Coefficients of exponential curve fit for atmospheric drag acceleration
v2rela	V_prop12	km/s	Estimated velocity relative to co-rotating atmosphere
vmag2	V_prop12	km/s	Magnitude of estimated relative velocity
rho2	V_prop12	kg/m^3	Estimated atmospheric density
AD	V_prop12	km/s^2	Estimated atmospheric drag acceleration vector
V3rela	V_prop12	km/s	Actual velocity relative to co-rotating atmosphere
vmag3	V_prop12	km/s	Magnitude of actual relative velocity
rho3	V_prop12	kg/m^3	Actual atmospheric density
AD3	V_prop12	km/s^2	Actual atmospheric drag acceleration vector
xdot	V_prop12	km/s^2	Differential equation (18x1 array)

B5. Input Parameters for Baseline (Reference) Case

The parameters used in the simulation include physical constants (mostly related to the earth) as well

as parameters used to describe the spacecraft, the initial orbit, the GPS, controller, and thruster.

5.1. Earth parameters:

All of the physical constants describing the gravitational body (Earth) are listed below.

- $\mu = 3.986004415 \cdot 10^5$ [km^3/s^2]
- $R_e = 6.3781363 \cdot 10^3$ [km]
- $W = 7.292115 \cdot 10^{-5}$ [rad/s]
- $g = 9.80665$ [m/s^2]

5.2. Spacecraft parameters:
- $C_d = 2.2$
- $A_c = 0.01$ [m^2]
- $M_{prop,0} = 0.09422$ [kg]
- $M_{dry} = 3.828$ [kg]

5.3. Orbital elements:
- $e_0 = 0.0022$
- $a_0 = 6603.1$ [km]
- $i_0 = 51.6274$ [deg]
- $Om_0 = 352.6165$ [deg]
- $om_0 = 76.1464$ [deg]
- $nu_0 = 323.6898$ [deg]

5.4. GPS uncertainty:
- SGR-05U receiver, Surrey Space Technology
  - $e\_r = 12.35 \cdot 10^{-3}$ [km]
  - $e\_v = 0.154 \cdot 10^{-3}$ [km/s]
- FOTON receiver, University of Texas
  - $e\_r = 1.2 \cdot 10^{-3}$ [km]
  - $e\_v = 0.07 \cdot 10^{-3}$ [km/s]
- poserr $= 11.547 \cdot 10^{-3}$ [km]
- velerr $= 0.14434 \cdot 10^{-3}$ [km/s]

5.5. Controller & EKF parameters:

- $Q\_e = 10$ (i.e. measurement update every 10 time steps)
- $C = 40$
- $q\_v = 0.000$ [km/s] (RMS of velocity process noise)
- $q\_a = 0.001 \cdot 10^{-3}$ [km/s^2] (RMS of acceleration process noise)

5.6. Thruster parameters:

- $Isp\_Busek = 500$ [s]
- $T_{max} = 0.175$ [mN]
- $T_{min} = 0.060$ [mN]

5.7. Solar power parameters:

- $P_0 = 8.33$ [W]
- $X_e = 0.9$
- $X_d = 0.9$
- $P_{EP} = 2$ [W]

The baseline case for the propagation on one orbital period takes approximately 300 seconds. The propagation of the full mission (~ 935 orbital periods) in the sunfire9 Linux cluster can take 7-10 days.